Implications of bank failures and fluvial erosion for gully development: Field observations and modeling

Erkan Istanbulluoglu, Rafael L. Bras, and Homero Flores-Cervantes

Department of Civil and Environmental Engineering, Massachusetts Institute of Technology, Cambridge, Massachusetts, USA

Gregory E. Tucker

Cooperative Institute for Research in Environmental Sciences and Department of Geological Sciences, University of Colorado, Boulder, Colorado, USA

Received 2 March 2004; revised 1 November 2004; accepted 10 January 2005; published 5 March 2005.

[1] Gully erosion is most commonly triggered by fluvial erosion following natural and anthropogenic disturbances or as a response to changes in climate and tectonic forcing and base level drop. Field observations attribute the headward growth and widening of many gully systems to gravitational mass-wasting processes of oversteepened sidewalls. Soil saturation, groundwater sapping, and tension crack development contribute to the instability. Recent landscape evolution models treat such mass failures as slope-dependent continuous sediment transport processes, sometimes conditioned on a slope threshold or with nonlinear dependence on slope gradient. In this study we first present an explicit physically based theory for the stability analysis of gully heads and walls. The theory is based on the force balance equation of an assumed planar failure geometry of a steep gully wall, with a potential failure plane dipping into the incised gully bed and tension cracks developing behind the scarp face. Then, we test the theory against field data collected in our field site in Colorado and against other published data. Second, the theory is implemented in a one-dimensional hillslope profile development model and the three-dimensional channel-hillslope integrated landscape development (CHILD) to study the effects of soil cohesion, erosion thresholds, and stochastic climate on the tempo of gully development and morphology. Preliminary results indicate that wider and shallower gullies develop and integrate, forming wide valleys, when soil cohesion is small. As soil cohesion increases, erosion slows down, gullies become deeper with vertical walls, and episodic mass failures occur. Differences in storm intensity-duration characteristics and erosion thresholds are predicted to have a significant impact on gully development. Vertical gully walls develop rapidly, and gullies enlarge by slab failures in a climate characterized by high-intensity, short-duration storm pulses. However, under low-intensity, long-duration storms, gullies quickly stabilize, and vertical walls are eliminated and rounded, forming diffusion-dominated hilltops. Erosion thresholds have a similar impact on the tempo of gully erosion but in the opposite direction. Lowering the erosion threshold enhances gully widening by slab failures. Gully walls stabilize when the erosion threshold is high due to a reduction in the erosion of the failure material on the toe of gully walls.

Citation: Istanbulluoglu, E., R. L. Bras, H. Flores-Cervantes, and G. E. Tucker (2005), Implications of bank failures and fluvial erosion for gully development: Field observations and modeling, *J. Geophys. Res.*, *110*, F01014, doi:10.1029/2004JF000145.

1. Introduction

[2] A gully is an incised, steep-sided channel, with an eroding headcut and slumping sidewalls [*Schumm et al.*, 1984; *Bradford and Piest*, 1980]. In the literature, the term ''gully'' is used for many different types of incised channels, which includes incisions in agricultural fields [*Poesen et al.*, 2003], shallow hillslope scars [*Montgomery*, 1999], and large entrenched dry channel systems [*Osborn and Simanton*, 1986]. Extensive field evidence reveals water erosion as the primary cause of gully development [*Mosley*, 1972; *Graf*, 1979; *Montgomery and Dietrich*, 1994]. Runoff erosion carves rills and forms headcuts that often retreat along the tracks of preexisting rills, in a process often called ''gullying'' [*Higgins*, 1990]. Undermining of headcuts by plunge pool erosion [*Bennett et al.*, 2000], piping and seepage erosion [*Dunne*, 1980; *Howard*

0148-0227/05/2004JF000145

and McLane, 1988; *Howard*, 1995], and mass wasting of sidewalls [*Dietrich and Dunne*, 1993; *Montgomery*, 1999] are among gullying processes commonly observed in the field.

[3] Gully erosion is usually attributed to changes in external and internal factors in the basin. External factors determine the magnitude of flow shear stress or stream power acting on the soil surface. These include tectonic uplift and base level lowering, climate forcing and natural and anthropogenic watershed disturbances.

[4] Changes in base level often form knickpoints in valley floors that migrate upslope toward headwater basins. Incision of valley floors forms terraces in which tributary gullies commonly cut and integrate into branching gully networks [e.g., *Schumm*, 1999]. Watershed disturbances usually increase runoff production and/or reduce erosion resistance of the soil surface, triggering gullies. Common disturbances include road building [*Wemple et al.*, 1996; *Croke and Mockler*, 2001] and removal of the protective surface vegetation cover due, for example, to grazing, forest clearing and wildfires [*Prosser and Soufi*, 1998; *Istanbulluoglu et al.*, 2002].

[5] Internal factors for gully erosion arise from the characteristic behavior of the erosion processes itself, such as feedbacks between topographic change, runoff generation and erosive power of overland flow [e.g., *Bull*, 1997]. There is often no clear distinction between internal and external factors in gully erosion. Gully development is cited as an example of equifinality in geomorphology, as a range of different processes and triggering mechanisms can apparently generate similar forms [*Cooke and Reeves*, 1976; *Schumm*, 1999].

[6] Large gully systems developed in the southwestern United States in the Late Quaternary have been the primary focus of gully erosion research in the United States since *Dodge* [1902] who proposed the term ''arroyo'' to describe the large steep-walled, flat-floored channels incised in valley floors [*Graf*, 1979]. Despite extensive field studies, which mostly concentrated on identifying the causes of arroyo development, a quantitative process-based theory to explain gully evolution is not yet available. Existing theory of channel or gully initiation describes overland flow induced headcut development on sloped surfaces. Simple topography-based threshold models developed for overland flow-controlled gully head locations predict the general inverse relationship between the observed area and local slope at channel heads [e.g., *Montgomery and Dietrich*, 1994; *Montgomery*, 1999], and explain the spatial variability of channel head locations when parameter uncertainty is incorporated through probability distributions [*Istanbulluoglu et al.*, 2002]. In contrast, headward advance of abrupt gully heads in low-gradient slopes are controlled by more complex gullying processes such as mass wasting, plunge pool erosion and seepage erosion that occur in conjunction with water erosion. The inherent complexity in gully development in low-gradient environments makes it difficult to develop simple topography-based models [*Montgomery*, 1999]. Some notable contributions, however, in numerical modeling of gully evolution include modeling planform evolution of drainage networks by groundwater seepage [*Howard and McLane*, 1988; *Howard*, 1995], and mass wasting of over steepened scarps [*Howard*, 1999; *Kirkby and Bull*, 2000; *Kirkby et al.*, 2003]. In these studies gullying processes are modeled implicitly using simple rules. For example in the latter models, mass wasting is treated as a diffusive-type process that varies nonlinearly with slope gradient, sometimes with a threshold [i.e., *Roering et al.*, 1999].

[7] Research questions that remain to be addressed to understand the complex nature of gully erosion include the following. (1) What are the implications of coupling different gully erosion processes (i.e., mass wasting, seepage erosion) with water erosion on the tempo of gully development, gully morphology and landscape response timescales? (2) Does soil type and vegetation cover affect gully erosion and favor any specific erosion processes over others? (3) What are the effects of climate variability and storm sequencing on gully incision rates and vegetation-erosion interactions? (4) What controls the observed episodicity in gully development, in which gullies form rapidly but may subsequently remain stable for many years? (5) Is episodic gully erosion a type of autocyclic process [*Schumm and Parker*, 1973] or does it require episodic external drivers?

[8] To begin addressing these questions, here we study gully development by water erosion and planar slab failures of gully banks using numerical modeling. Slab failures often result from undercutting of gully banks by water erosion and development of vertical tension cracks in the upper part of the bank. Such failures are commonly observed in incising arroyos in the southwestern United States [*Bull*, 1997], as well as in many lowland streams [e.g., *Thorne*, 1999; *Dapporto et al.*, 2003]. Figure 1 shows a typical slab failure (indicated by the left arrow) triggered in a deep gully in Fort Carson, Colorado. A large tension crack developed from the top to the bottom of the gully wall (indicated by the right arrow) is also seen in the figure. Tension cracks usually extent down to the failure plane, which often passes through the base of the bank, shortening the length of the failure surface. Storm water that infiltrates the cracks produces hydrostatic pressure on the slab, and generates uplift forces along the failure plane. Slab failures occur when gravitational forces exceed the shear strength of the soil [*Bradford and Piest*, 1980]. Failed material deposits at the toe of the bank, as seen in the bottom part of the picture in Figure 1, and the bank remains stable until the failed material erodes by the flow in the channel, slope wash, soil creep and bioturbation [*Thorne*, 1999].

[9] A number of studies have used geotechnical methods to analyze mass wasting in river banks. These include testing stability equations for different failure geometries using in situ bank materials [*Bradford and Piest*, 1980; *Thorne*, 1999; *Dapporto et al.*, 2003], and modeling fluvial in-channel processes (i.e., sediment sorting, evolution of bed topography) in concert with gravitational bank processes to explore the governing factors in channel adjustment and evolution in lowland streams [*Simon and Darby*, 1997; *Darby and Thorne*, 1996; *Darby et al.*, 2002]. These studies, however, are only limited to in-channel processes in large rivers without the

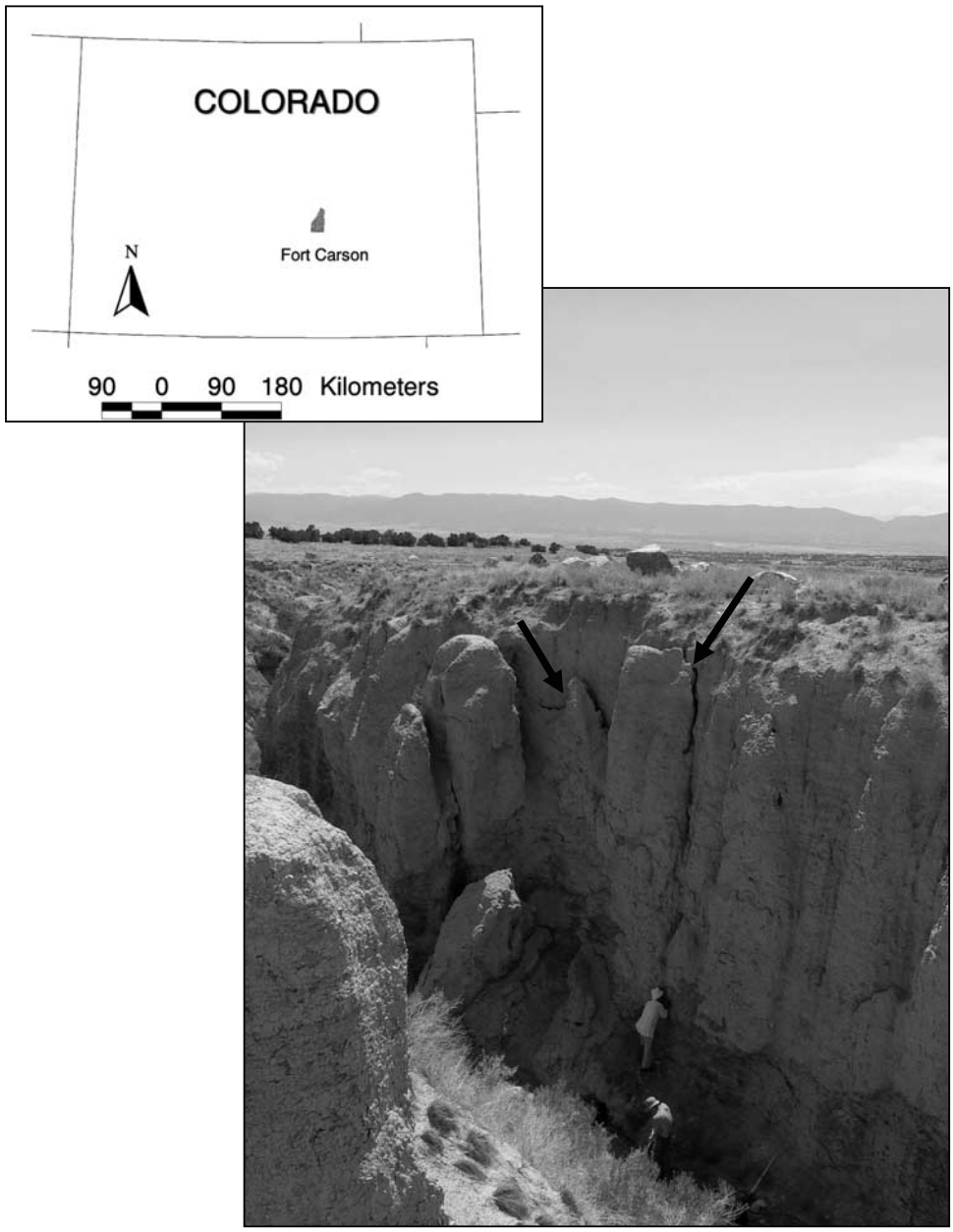

Figure 1. A deep gully subject to gravitational failures located in Fort Carson, Colorado. The gully was surveyed for testing the slab failure model presented in section 2. A slab failure is indicated by the left arrow. A large tension crack developed from the top to the bottom of the gully wall is indicated by the right arrow.

integration of channels with hillslope systems in a larger geomorphic landscape context.

[10] In this paper, we first present a physically based approach for the initiation of planar slab failures based on a force balance equation of an assumed failure geometry. We then describe the field observations to test the physical approach. Finally we implement the theory in two landscape evolution models. The first model is a one-dimensional finite difference approach developed to investigate the effects of slab failures on profile development in the absence of any topographic influence (i.e., convergence and divergence of water and sediment). The second model is the channel-hillslope integrated landscape development (CHILD) model, which is a three-dimensional computational framework for modeling landscape evolution [*Tucker et al.*, 2001a, 2001b].

2. Theory

[11] In general, the rate of change of topographic elevation, $\partial z/\partial t$, is due to the difference between a source term, T_U, that provides the sediment mass to the system, such as base level lowering or tectonic uplift, and an erosion/deposition term based on the divergence of sediment (and

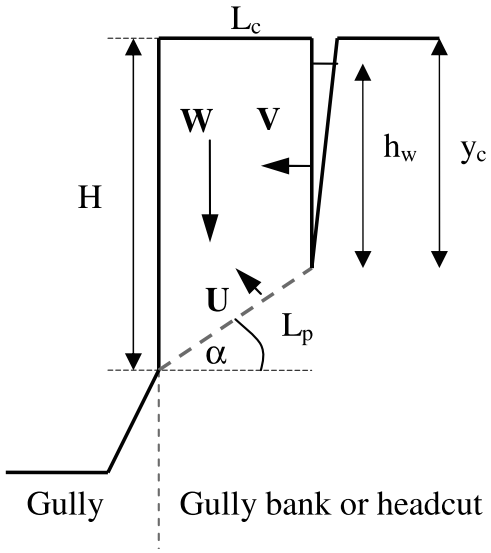

Figure 2. Schematic of the assumed geometry of a failure block used in the slab failure model. Arrows indicate the different forces acting on the failure block. Symbols are described in the text in section 2.1.

solute, where applicable) flux per unit width of a surface, q_s:

$$\frac{\partial z}{\partial t} = T_U - \nabla q_s, \tag{1}$$

where z is surface height above a datum and t is time [e.g., *Kirkby*, 1971; *Willgoose et al.*, 1991; *Tucker and Bras*, 1998]. In the equation, T_U has dimensions of (L/T) and q_s of (L^2/T). In numerical solutions of erosion and deposition over a finite area, the divergence of sediment flux, ∇q_s is approximated as the difference between the outgoing and the incoming sediment fluxes divided by the size of the model element. The sediment flux term in equation (1) can combine a number of different erosion and sediment transport laws with different functional forms, including diffusive (e.g., soil creep, rain splash) and advective (fluvial and landsliding) processes [*Dietrich et al.*, 2003]. The slab failure mechanism described in the next section represents a new process that contributes to the sediment flux term in equation (1).

2.1. Slab Failures

[12] Planar failure geometry of a steep wall with a potential failure plane dipping to the channel bed and a tension crack developed at the back of the vertical face is given in Figure 2. Similar failure geometries, sometimes more complex, have been used in the stability analysis of river channels [i.e., *Darby and Thorne*, 1996; *Thorne*, 1999]. On the basis of the Coulomb equation, the factor of safety (FS) the ratio of resisting to driving forces acting on the failure plane, is expressed as

$$\mathrm{FS} = \frac{CL_p + (W\cos\alpha - U - V\sin\alpha)\tan\phi}{W\sin\alpha + V\cos\alpha}, \tag{2}$$

where C is soil cohesion acting along the failure plane (Pa), L_p is the length of the failure plane (m), W is the weight of the block per unit width, U is the hydrostatic uplift force per unit width due to positive pore pressure along the failure plane, V represents hydrostatic pressure of the water in the crack and ϕ is the soil friction angle. On the basis of the failure geometry, we can express W, V and U as

$$W = 0.5\rho_s g(H + y_c)L_c, \tag{3a}$$

$$V = 0.5\rho_w g h_w^2, \tag{3b}$$

$$U = 0.5\rho_w g h_w L_p, \tag{3c}$$

where H is the height of the vertical scarp face, y_c is the depth of the tension crack, h_w water depth in the tension crack, ρ_s and ρ_w are soil and water density respectively, L_c is the distance from the headcut face to the crack, and L_p is the length of the failure plane. Both L_c and L_p can be calculated based on the block geometry as

$$L_c = (H - y_c)/\tan\alpha \tag{4a}$$

$$L_p = (H - y_c)/\sin\alpha, \tag{4b}$$

where α is the angle of the potential failure plane, commonly taken as $\alpha = 45 + \phi/2$ [*Selby*, 1993; *Dietrich and Dunne*, 1993]. The stability model can be cast in the form of a instantaneous sediment transport law per unit width of scarp:

$$q_s' = \begin{cases} L_c(H + y_c)/2 & \mathrm{FS} < 1 \\ 0 & \mathrm{FS} \geq 1 \end{cases}, \tag{5}$$

where q_s' is sediment flux per unit width per event across a plane normal to the failure surface at the base of the scarp.

[13] We analyze equation (2) under three different conditions to obtain simple expressions that can be used to interpret field observations. The first case concerns the maximum height of a vertical soil block that develops in the absence of cracks ($y_c = 0$), in unsaturated material ($h_w = 0$). In this case the failure plane extents up to the soil surface and the instability of the block is due to an increase in the weight of the block as base level drops. Setting FS = 1 and solving for H, the maximum critical height that the block can attain, $H_{\max}$ is

$$H_{\max} = \frac{2C}{\rho_s g\cos\alpha}[(\sin\alpha - \cos\alpha\tan\phi)]^{-1}. \tag{6}$$

The second case considers the development of cracks in dry soils, for which $y_c > 0$ and $h_w = 0$. Solving equation (2) for H when FS = 1, and substituting (6) in this expression, one can write the critical height of a slab with dry cracks developed at the back of the scarp face, $H_{C-\mathrm{Dry}}$ as

$$H_{C-\mathrm{Dry}} = \frac{2C}{\rho_s g\cos\alpha}[(\sin\alpha - \cos\alpha\tan\phi)]^{-1} - y_c. \tag{7}$$

This is similar to the Culmann equation for rock wedge instability [i.e., *Selby*, 1993]. Both (6) and (7) have been used in the literature to study maximum height of channel walls [*Bradford and Piest*, 1980] and predict the maximum ridge-valley relief in mountains subject to bedrock landsliding [*Schmidt and Montgomery*, 1995; *Densmore et al.*, 1998].

[14] Equation (7) requires information on crack depths. This can be difficult to obtain in the field as crack sizes could vary significantly both in time and in space, especially as the scarp height grows. Previous work suggests the use of a crack depth equal to half the wall height in the absence of field observations [*Selby*, 1993; *Bradford and Piest*, 1980]. In the model, we assume y_c proportional to H. For the critical height of the slab with a dry crack this gives $y_c = \varepsilon H_{C-\mathrm{Dry}}$ $(0 < \varepsilon < 1)$. Substituting this expression into (7), we can write $H_{C-\mathrm{Dry}} = H_{\max}/(1 + \varepsilon)$.

[15] In the other extreme case, the critical height is attained when tension cracks are entirely full with water and thus V and U are at their maximum values. Here, substituting $h_w = y_c = \varepsilon H_{C-\mathrm{Wet}}$, into equations (3a), (3b), (3c), and (2), setting FS = 1 and solving for H, we get

$$H_{C-\mathrm{Wet}} = \frac{2C}{\rho_s g \cos\alpha}(1-\varepsilon)\left\{\left(1-\varepsilon^2\right)(\sin\alpha - \cos\alpha\tan\phi) + \frac{\rho_w}{\rho_s}\varepsilon\tan\alpha\left[\frac{(1-\varepsilon)\tan\phi}{\sin\alpha} + \varepsilon(\cos\alpha + \sin\alpha\tan\phi)\right]\right\}^{-1}. \tag{8}$$

Equation (8) is only applicable in areas where either overland flow discharge or flood discharge within the channel provides enough water to fill the cracks. For $\varepsilon = 0$, this equation predicts $H_{\max}$ given by (6).

[16] When the tension cracks are partially filled with water, we expect a dependence between critical height for slab failures and upslope contributing area, which acts as a surrogate for water input into the crack by overland flow during a rainstorm or snowmelt event. Here we derive this dependence based on two simple assumptions. We assume that a tension crack has a limited capacity to infiltrate water along its walls, and define flux capacity per unit length of a crack, q_c, as a function of water depth in the crack:

$$q_c = I_c h_w, \tag{9}$$

where, I_c is the horizontal infiltration capacity (L/T) per unit depth of a crack in unit width. Assuming steady state, spatially uniform runoff generation, the water flux is

$$q = \langle P - I_s \rangle A, \qquad P > I_s, \tag{10}$$

where P is rainfall rate and I_s is vertical soil infiltration capacity, and A is contributing area per unit contour width. We solve for the water depth in a crack by equating overland flow discharge to crack flux capacity. This gives h_w proportional to specific catchment area:

$$h_w = \Omega A \qquad \Omega = \langle P - I_s \rangle / I_c \tag{11}$$

for $P > I_s$ and $h_w \le y_c$, where Ω is the ratio of runoff rate to crack infiltration capacity (both in units of L/T) and defines a nondimensional parameter that relates upslope contributing area to water depth in the cracks. In equation (11), y_c defines an upper bound to h_w, and the crack overflows when $h_w > y_c$. In our steady state hydrology assumption, completely filling of a crack requires that the unit contributing area is higher than or equal to a threshold area for saturation. Assuming $h_w = y_c = \varepsilon H$ in the left-hand side of equation (11) and solving for area gives the threshold area for filling cracks, A_c:

$$A \ge A_c = \frac{\varepsilon H}{\Omega}. \tag{12}$$

[17] This threshold area poses an upper limit to the control of area on hydrostatic and seepage forces that tend to destabilize gully walls (equation (2)). Any additional area increase (i.e., moving downslope along a hollow axis) would have no influence on the triggering of slab failures. In this case failures occurs when scarp height is greater than $H_{C-\mathrm{Wet}}$ derived in equation (8).

[18] When the unit contributing area is smaller than the threshold area for full saturation of the crack, then the maximum scarp height becomes a function of unit contributing area. We define a critical threshold area required for the instability of a given scarp height, by substituting (11) into (3b) and (3c) and these equations into (2), equating FS to 1 and rearranging, that gives a quadratic expression for a unit contributing area threshold, A_t:

$$XA_t^2 + YA_t + Z = 0 \qquad A_t \le A_c = \frac{\varepsilon H}{\Omega}. \tag{13}$$

For $Y^2 > 4XZ$, A_t has two real number solutions. Failure will occur when the upslope contributing area of a scarp face is greater than the threshold area, $A_t < A < A_c$. Constants of the quadratic function are

$$X = (\sin\alpha + \cos\alpha/\tan\phi)\Omega^2, \tag{14}$$

$$Y = L_p\Omega, \tag{15}$$

$$Z = \frac{2}{\rho_w g}\left[W\left(\frac{\sin\alpha}{\tan\phi} - \cos\alpha\right) - \frac{CL_p}{\tan\phi}\right]. \tag{16}$$

[19] Figure 3 demonstrates the solution space for equation (13) defined in terms of scarp height and unit contributing area based on equations (6), (7), (8), (11), and (13). Three horizontal lines divide the domain to different regions conditioned on the existence of tension cracks and water level in the cracks. In the figure, the dashed line separates regions of filled and partially filled cracks by plotting the threshold area for crack saturation as a function of scarp height (equation (12)). In the partially filled region, failure is controlled by both unit contributing area and scarp height. For cases when there are no cracks, completely dry cracks, or completely saturated cracks instability is controlled only

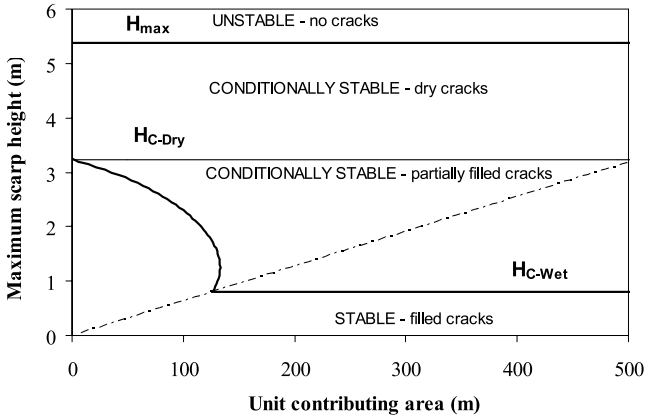

Figure 3. Scarp height as a function of contributing area, showing the regions that define different conditions for headcut stability. The dash-dotted line plots equation (12), separating the domain to regions of filled and partially filled cracks. From the top to the bottom of the figure, horizontal lines plot the maximum critical height, $H_{\max}$ (equation (6)), and the critical height with dry, $H_{C-\mathrm{Dry}}$, and filled, $H_{C-\mathrm{Wet}}$, tension cracks using equations (7) and (8), respectively. The curve between the $H_{C-\mathrm{Wet}}$ and $H_{C-\mathrm{Dry}}$ regions plot equation (13), relating the critical scarp height inversely to contributing area. Model parameters are C = 10 kPa, ε = 0.66, and Ω = 0.004.

by the scarp height, defined by $H_{\max}$, $H_{C-\mathrm{Dry}}$ or $H_{C-\mathrm{Wet}}$ respectively.

[20] Figure 4 shows the sensitivity of the model to different values of C, Ω and ε. In all three plots, the dashed line shows the relationship between the area required for crack saturation and the maximum scarp height (equation (12)). In Figure 4a, an increase in C shifts the curves to higher threshold height values for both filled and partially filled crack conditions, increasing the size of the tension cracks and consequently the area required for crack saturation. A larger Ω can be interpreted as either a larger runoff rate or a smaller crack infiltration capacity, both of which reduce the catchment size required to fill tension cracks. In Figure 4b the slope of the dashed line increases for larger values of Ω (equation (12)). The model has a more complex response to changes in ε, the ratio of crack depth to scarp height, as all the model components except Ω are related to ε. Note that when $\varepsilon = 0$, there is no crack development, $y_c = 0$, and the threshold scarp height is obtained from equation (6) (Figure 4c). Threshold area for completely filling a crack is directly proportional to ε, and thus for a given scarp height a larger catchment area for crack saturation is needed for large values of ε. This decreases the slope of the saturation threshold line (dashed line in Figure 4c), and leads to a shorter failure plane, higher seepage and hydrostatic forces, and a smaller block weight, since $W \propto H^2 - (y_c = \varepsilon H)^2$. All of these effects reduce the threshold scarp height. In Figure 4c, a fourfold increase in ε leads to a fourfold decrease in $H_{C-\mathrm{Wet}}$, while significantly changing the shape of the threshold envelope. Interestingly, in the unsaturated region for $\varepsilon = 0.8$, the relationship between scarp height and contributing area gives a maximum value. Above the maximum point, stability is predominantly driven by a higher block weight, reducing the source area size for critical levels of water in the tension crack. Below the maximum point, depth of tension crack reduces so that it is filled to a critical water level for slab instability with a smaller contributing area.

2.2. Diffusive and Advective Processes

[21] In order to model the combined effects of slope-limiting rapid erosion (i.e., small-scale landsliding) [*Roering et al.*, 1999] and soil creep, sediment flux due to diffusive processes is written as

$$q_{sD} = \begin{cases} K_d S + \infty & S > S_t \\ K_d S & \end{cases}, \tag{17}$$

where, S_t is a threshold slope for small-scale shallow landsliding of talus deposits, K_d is diffusion constant, and ∞ represents instantaneous sliding [*Tucker and Bras*, 1998]. In cohesive soils, the threshold angle is larger than 90°, so that vertical scarps develop. In the model, equation (17) is not applied to vertical scarps where sediment release is by slab failures. Instead, this equation is used for hillslopes and for unconsolidated failure deposits that form talus slopes at the toe of the gully banks. The threshold angle provides an upper limit to the gradient of the talus slope with any additional failure material released from the scarp by slab failures is transported across the talus slope without deposition.

[22] In this paper runoff erosion is assumed to be detachment limited. This assumption implies that detachment capacity is everywhere significantly smaller than the carrying capacity of water, and erosion is only limited by local ability of water to erode the soil surface [*Howard*, 1999]. Detachment-limited erosion has been incorporated in landscape evolution models for modeling evolution of headwater basins [e.g., *Howard*, 1994, 1999]. Detachment capacity is calculated as a function of overland flow shear stress, τ, in excess of a critical shear stress threshold, τ_c:

$$\frac{\partial z}{\partial t} = -k_e(\tau - \tau_c)^p, \qquad \tau > \tau_c \tag{18}$$

$$\tau = \beta\langle P - I_s\rangle^m A^m S^n, \qquad P > I_s, \tag{19}$$

where k_e is soil erodibility, p is a parameter, traditionally $p = 1$ in agricultural soil erosion models, but as newer field evidence suggests could be higher up to 2.5 on steep slopes, and under high shear stresses [e.g., *Nearing et al.*, 1999], and ρ_w is water density. Overland flow shear stress is written as a function of discharge and slope (equation (19)), assuming overland flow is hydraulically rough, with roughness independent of Reynolds number and using Manning's equation to calculate flow velocity, that gives m = 6/10, n = 7/10, and $\beta = \rho_w g n_t^{6/10}$, where n_t is the Manning's roughness coefficient for unchanneled overland flow [e.g., *Willgoose et al.*, 1991].

3. Field Observations

[23] We test the theory described above using our field measurements in a gully system developed in Fort Carson,

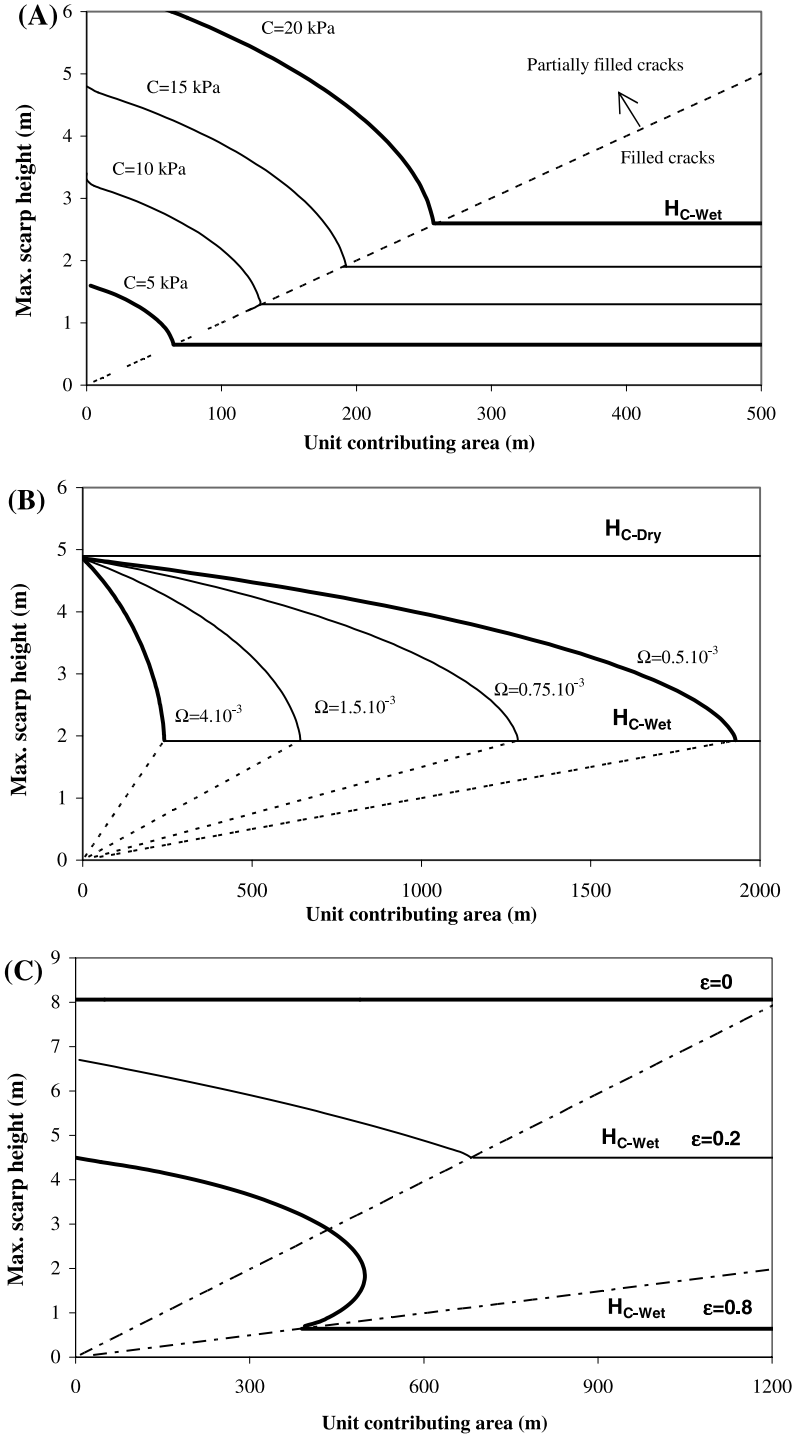

Figure 4. Sensitivity of the model in the area–scarp height solution space for the following: (a) soil cohesion, C, for values of 5, 10, 15, and 20 kPa using $\Omega = 0.004$ and $\varepsilon = 0.5$; (b) hydrology parameter, Ω, of 0.0005–0.004 for $C = 15$ kPa and $\varepsilon = 0.5$; and (c) fraction of crack depth to headcut height, ε, for values of 0–0.8 using $C = 15$ kPa and $\Omega = 0.001$.

south of Colorado Springs, at the foot of the Colorado Front Range (Figure 1), and other published data from the literature. Fort Carson's physiography ranges from low-relief piedmont slopes to rugged foothills, and is underlain primarily by Mesozoic to Cenozoic sedimentary rocks. The mean annual precipitation in the area is 500 mm, over a third of which falls during July and August as short-duration, high-intensity thunderstorms with 5 min rates up to 100 mm/hr. The soils are silty clay and clay loam in the plains and gravelly sandy loam with scattered rocks on the hilltops and steeper hillslopes. Gullies in Fort Carson and in the surrounding regions are typically rectangular to U-shaped in cross section. They have distinct headcuts and sidewalls subject to slab failures. Figure 1 shows a typical

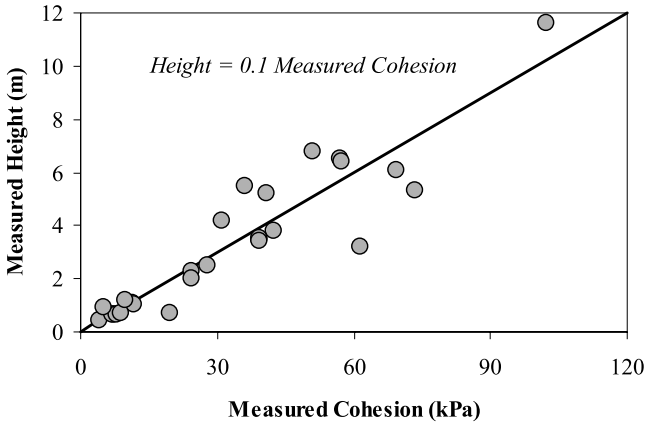

Figure 5. Observed vertical bank height as a function of measured soil cohesion in Fort Carson, Colorado. Cohesion values are the averages of six measurements at each site. The line fits a linear relationship between the measured cohesion and the bank height.

deep gully developed in the area. Note the development of a large tension crack from top to bottom of the gully wall (indicated by the right arrow). Tension cracks contribute to the trigger of gravitational failures as seen between the two hanging blocks (indicated by the white arrow). Failed material forms talus slopes with average slope angles of 35°.

[24] We measured vertical height of gully banks above the talus, soil cohesion, and talus gradient. Cohesion was measured on bank tops (approximately 15 cm from the bank edge) and on vertical bank sides, using a shear vane with three repetitions. In locations where a tension crack was observed at the back of the vertical face, the depth of the crack was added to the vertical height following equation (7). Because our initial aim was to test the theory for unsaturated material (equations (6) and (7)), all the observations were collected at locations where signs of storm runoff convergence from gully sides were absent or insignificant. Soil saturated hydraulic conductivities in the area were measured around gully headcuts, gully bottoms and unchanneled surfaces in the valley fills using a Guelph Permeameter. Measured saturated hydraulic conductivity values range from 10 to 100 mm/hr.

[25] Figure 5 shows the observed vertical height of gully sidewalls against the average measured in situ soil cohesion at each location. The linear relationship between height and cohesion is consistent with equation (6). However, when the field work was conducted in early fall, the soils were almost entirely dry. This suggests that an important portion of the measured cohesion can be attributed to high values of soil suction of dry soils [*Collison*, 1996, 2001]. *Simon et al.* [2000] monitored soil cohesion and soil suction in a field site in the southeastern United States. Their data showed high correlations between the observed soil suction and soil cohesion. During their monitoring period soil cohesion produced by soil suction increased from a winter-spring average value of ~5 kN/m up to ~25 kN/m by the end of the monitoring period in August. As this literature also suggests, a height-limiting cohesion value for the gully banks in our field area would be smaller than the values observed in the field. In order to adjust the observed soil cohesion to plausible values during the times of slab failures (i.e., values during floods or after prolonged wetting periods when soil moisture is high and suction forces are low) we used field evidence from a few recent failures on gully sidewalls to back-calculate cohesion values in the time of failure using equation (7). In one failure for example, a void of approximately 3.4 m height, 1 m width and 0.35 m deep was identified along a deep gully, with a deposit originating from this failure on the toe of the gully bank below the void. Total height of the sidewall was 4.4 m including a steep talus slope. We used an average measured talus slope angle of 35° for ϕ in equation (7) and assumed that ρ_s = 1850 kg/m^3. The back-calculated cohesion values are approximately five times lower than those observed in the field. This difference is within the expected range of variation in the soil cohesion between dry and wet soils [e.g., *Simon et al.*, 2000]. For example, *Collison* [1996] reported up to threefold increase in soil strength under larger soil suction conditions for marl soils. On the basis of this field evidence we corrected all our cohesion measurements to wetter field conditions by dividing them by 5. Corrected cohesion values range between 0.85 kPa and 21 kPa. We then calculated the potential maximum stable height that adjusted cohesion values can support using equation (7), and compared this to the observed heights (Figure 6). Despite the uncertainties, this simple model provides a reasonable agreement with field observations.

[26] Overland flow is an important factor in headcut retreat in gullies draining convergent topography [*Montgomery*, 1999]. In this case, the theory presented above predicts an inverse relationship between headcut height and drainage area when tension cracks are partially filled with storm water (Figure 3). In our field site in Fort Carson, many of the surveyed gully heads lie just downslope from dirt roads, where drainage ditches and other human disturbances (i.e.,

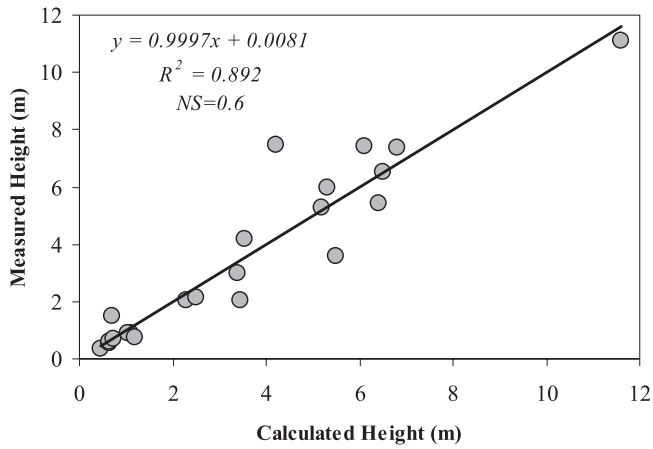

Figure 6. Comparison of the calculated vertical bank height using equation (7) to the observed height in the field. In the calculations, adjusted cohesion values are used to represent soil cohesion during wetter conditions. The line plots the linear regression line between the calculated and observed stable bank heights. NS is the Nash-Sutcliffe error measure [i.e., *Gupta et al.*, 1998], suggesting that the model, with observed soil cohesion inputs, can explain 60% of the variability in the observed bank heights.

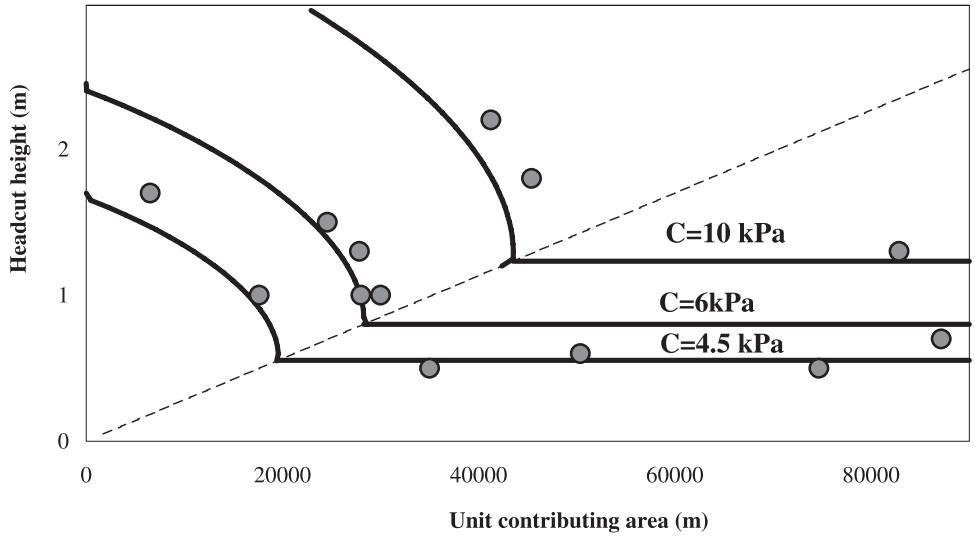

Figure 7. Comparison of the relationship between headcut height and contributing area per unit headcut width using data reported by *Nyssen et al.* [2002]. Horizontal lines plot equation (8), and the curves plot equation (13) for calibrated model parameters. The dashed line separates the domain to saturated and unsaturated crack regions.

tracked vehicle imprints on and around the road sides) strongly influence the drainage patterns. Because of the difficulty in measuring drainage area in our field area, here we used data from another published study to test the theory in predicting the relationship between the critical headcut height and upslope contributing area.

[27] *Nyssen et al.* [2002] tabulated drainage areas, local slopes, widths and heights of 11 headcuts in the highlands of Ethiopia. Gullies were incised on moderately sloped (~10%) rangelands with cohesive soils. Figure 7 shows the area-headcut height relationship for the gully heads and plots the theory fitted to the field data. The unit contributing area of each gully head is obtained by dividing the total area draining to the gully head by the width of the headcut. Two model parameters Ω and C are calibrated to provide a reasonable correspondence between the data and the theory in the absence of detailed information on climate, hydrology and soil cohesion in the field areas. We derive a value of $\Omega = 2.8 \times 10^{-5}$ and used three cohesion values: 4.5 kPa, 6 kPa and 10 kPa. Different cohesion values can be justified by recognizing the inherent variability of soil cohesion in the field and the effects of soil moisture on soil cohesion. In Figure 7, the dashed line separates the plot into unsaturated and saturated regions for cracks. The curves above the dashed line plot equation (13) and the straight lines below the dashed line plot equation (8). The gully heads plotting above the dashed line are predicted to be unsaturated at the time of failure, showing a negative dependence between source area and the headcut height (equation (13)). The gully heads plotting below the dashed line show no dependence between headcut height and drainage area suggesting crack saturation at the time of those failures.

4. Model Applications

4.1. One-Dimensional Profile Evolution

[28] We used a one-dimensional landscape evolution routine to explore the implications of slab failures on landscape morphology under different modes of detachment-limited erosion. The model uses a finite difference algorithm to solve a detachment-limited erosion law, and the slab failure equation described in section 3. Here, for the sake of simplicity and to make our results comparable with the previous work, we employed the simplest and most commonly used form of the detachment-limited erosion law, in which erosion rate is a power function of contributing area and slope. Substituting (19) into (18), assuming discharge linear to drainage area, and neglecting the threshold term τ_c gives [*Howard*, 1980]

$$\frac{\partial z}{\partial t} = -KA^M S^N, \tag{20}$$

where K is an incision efficiency constant that lumps information related to climate, soil erodibility and flow roughness. For overland flow, the exponents are $M = mp$ and $N = np$. As first demonstrated by *Rosenbloom and Anderson* [1994] equation (20) can be written in the form of a nonlinear kinematic wave equation, $\partial z/\partial t = -\delta|\partial z/\partial x|$, where δ is the wave speed, $\delta = Ka^M S^{N-1}$, and defines the upstream migration rate of a knick point along a river profile. This was used by *Whipple and Tucker* [1999] to derive an expression for the landscape response timescales to tectonic perturbations. Solutions to equation (20) take the form of traveling waves with three different types of transient behavior corresponding to $N < 1$, $N = 1$, and $N > 1$ with emergence of shock waves in the solution when $N \neq 1$ [*Weissel and Seidl*, 1998; *Tucker and Whipple*, 2002].

[29] Here we perform simulations with different shear stress exponents, p, in order to explore the implications of slab failures on one-dimensional profile forms. One-dimensional finite difference solutions were calculated using 100 nodes that represent an initial condition of a flat plateau terminating with an abrupt drop. The toe of this vertical face is an open boundary where any sediment reaching this location is taken out of the domain. Drain-

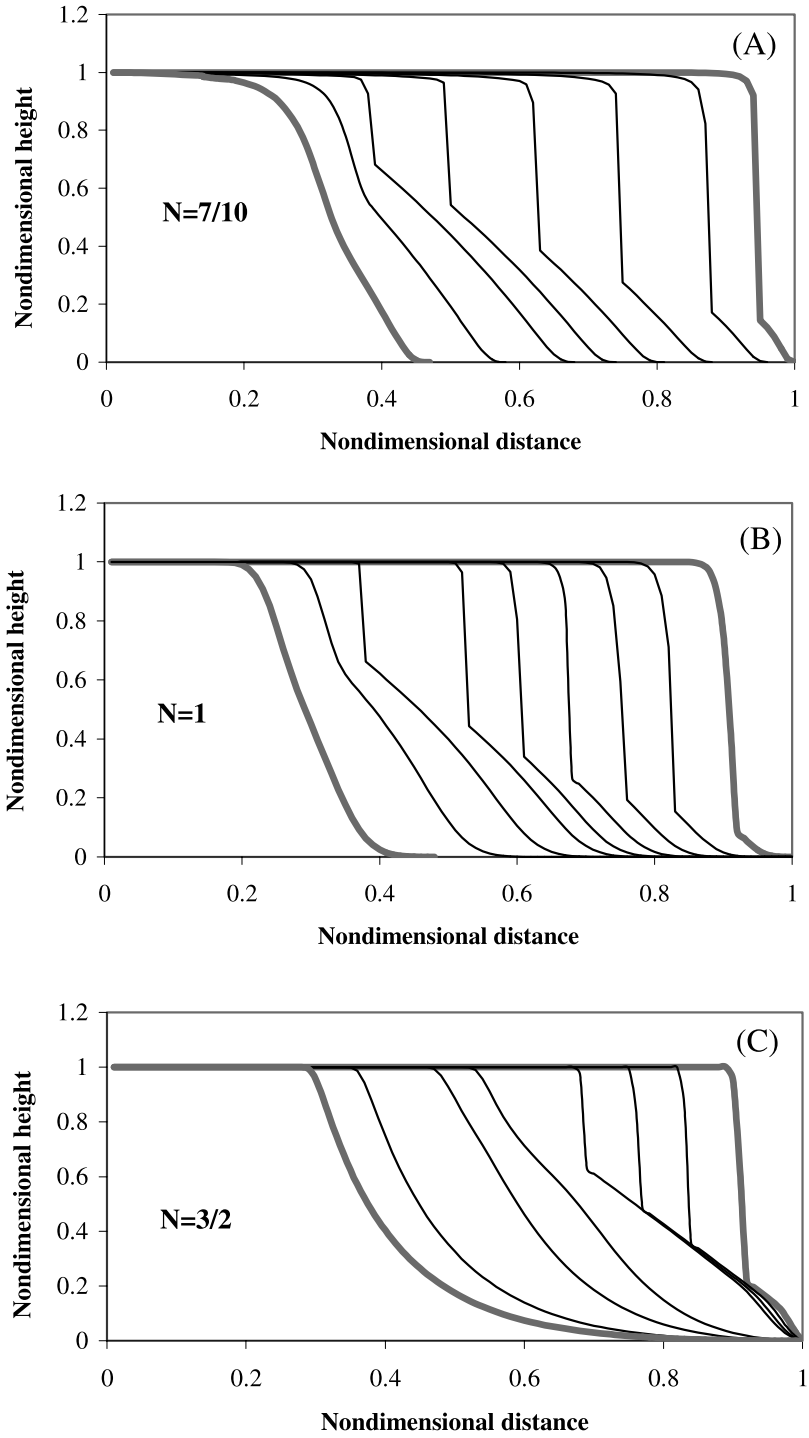

Figure 8. One-dimensional evolution of an elevated plateau surface under the action of slab failures and detachment-limited fluvial erosion. Each channel profile corresponds to several time slices during the model runs for (a) $N = 7/10$, (b) $N = 1$, and (c) $N = 3/2$. The thick, shaded lines highlight the change in the profile during the simulation.

age area is assumed to increase linearly toward the open boundary. The numerical procedure is executed from downstream (open boundary) to upstream nodes. Mass wasting of vertical scarp face is modeled in conjunction with detachment-limited wash erosion. In modeling slab failures, the height of each node, H is calculated using a forward difference method. Slab failure occurs when $H > H_c$. Each failure removes exactly enough material to reduce the local slope to the angle of the potential failure plane, α (equation (3)). The amount of soil released from each failure is routed downslope. When cascading debris reaches a node where $S < S_t$, just enough material is deposited to increase the downstream slope to S_t. For each failure, this process is repeated recursively until all

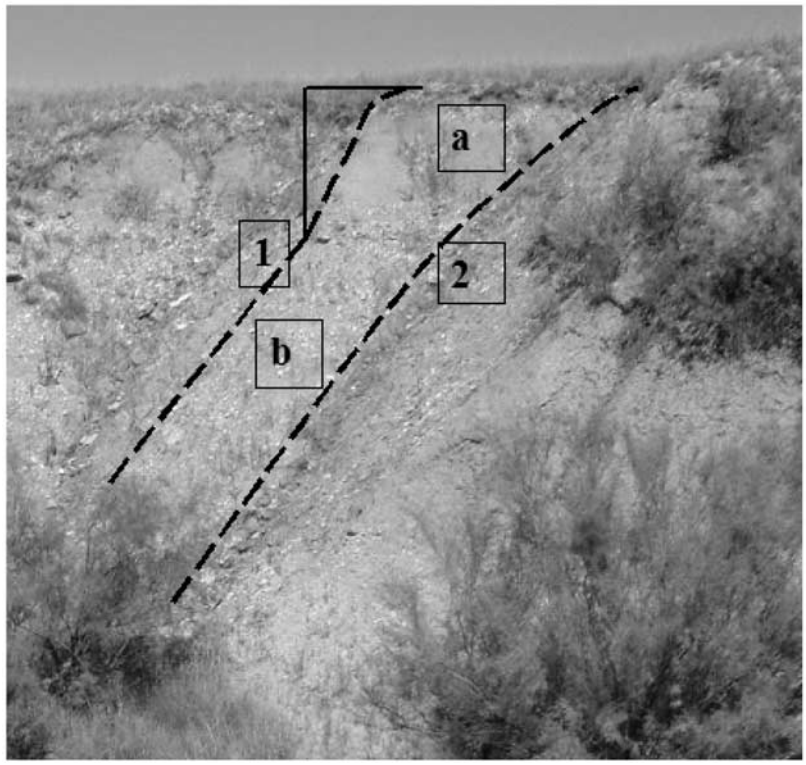

Figure 9. A gully bank observed in the field. Slab failure is not an active mechanism in the current time. From the top, "a" is a former vertical scarp face currently eroding by soil wash and creep, and "b" is a talus slope. The dashed lines mark profiles. Active soil wash (2) has eroded the vertical face, forming a rounded hill crest.

the failure material has either been deposited or transported out from the open boundary. For the sake of simplicity, we set $S_t = \tan \phi$, where $\phi = 35°$.

[30] Figure 8 shows scarp profiles plotted in several time step intervals throughout the simulation. Slope exponents used in the erosion model are $N = 7/10$, $N = 1$, and $N = 3/2$ (equation (20)). For overland flow, these values correspond to excess shear stress exponents of $p = 1$, $p \approx 3/2$, and $p = 5/2$, respectively that are within the range reported in laboratory and field studies. In all three of the experiments, profile evolution is controlled by the interplay between the detachment-limited erosion that tends to eliminate slopes and erase topography (in the absence of any thresholds), and falling debris from the vertical face due to slab failures that tends to maintain a critical slope angle. During the initial time steps of the simulations, a talus slope develops at the foot of the plateau. As failures continue, the vertical face is progressively replaced by the upward expansion of the gentler talus slope. Slope replacement continues until the height of the vertical cliff is less than the critical height for the occurrence of slab failures, whereupon failures cease and soil wash erode the vertical scarp face in time.

[31] The differences in the hillslope profiles plotted in Figure 8, solely reflect the effects of the nonlinear dependence of local runoff erosion to the local slope gradient. When $N < 1$, the speed of the erosion wave is high on shallow slopes as the wave speed, δ, varies inversely with S, leading to rounded scarp edges at the top, and abrupt slope breaks at the base of the retreating profiles. When $N = 1$, wave speed does not depend on slope, and the model yields a profile that maintains its characteristic form as it erodes by parallel retreat. For the case when $N > 1$, wave speed is a nonlinear function of local slope. The erosion rate slows down quickly as slopes decrease (i.e., no erosion at the top of the scarp), causing higher retreat rates on steeper upper slopes that results in the formation of sharp edges at the top of the scarp face. Slopes free of scarps show declining graded profiles. In all three simulations, once the vertical wall is removed, further shaping of the hillslope profile is controlled by fluvial erosion, as manifested by the emergence of typical characteristics of detachment-limited erosion depending on the value of N [i.e., *Tucker and Whipple*, 2002].

[32] Simulated one-dimensional (1-D) profiles can be used as a guide to differentiate between the different values of slope exponents of wash erosion model in a real topography. Figure 9 shows a section of a sideslope of a gully, in which a relict scarp face (indicated by "a"), at present eroding by wash erosion and hillslope diffusion, and a talus slope (indicated by "b") can be observed. The solid line reconstructs the shape of the former vertical scarp face. The dashed line indicated by "1" shows the profile of the current talus slope, located on a topographic nose that divides two small swales formed on both sides of the slope by soil wash. The dashed line indicated by "2" marks the axis of a small swale effectively eroding by wash erosion, with an armored bed and litter deposits. A greater rate of soil wash in 2 has eroded the scarp face, forming a much rounded hilltop than in 1. Both profiles closely resemble the

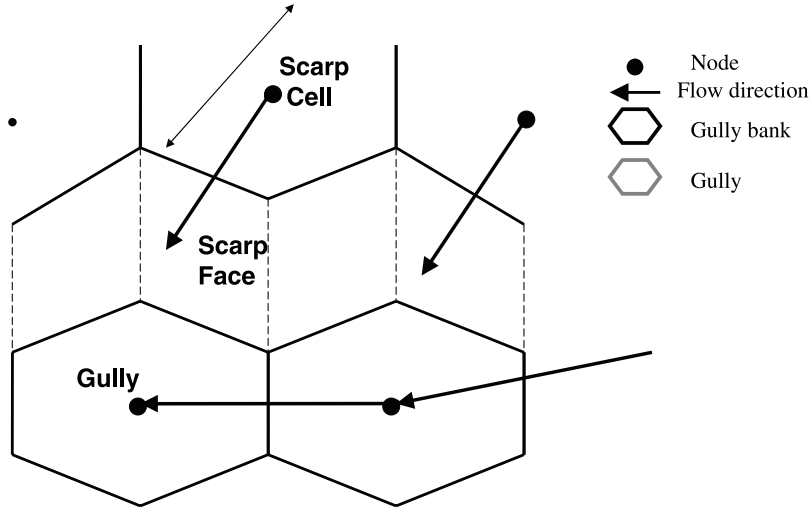

Figure 10. Illustration of the positioning of the scarp face and scarp cell in a gully bank, represented by Voronoi cells in the channel-hillslope integrated landscape development (CHILD) model. Arrows show the steepest descent flow and sediment routing from node to node.

simulated 1-D hillslope profiles during the final stages of the simulation (i.e., the last three profiles) in Figure 8a.

4.2. Gully Erosion Modeling Using the Channel-Hillslope Integrated Landscape Development (CHILD) Model

[33] The channel-hillslope integrated landscape development (CHILD) model [*Tucker et al.*, 2001a, 2001b] is used to investigate the effects of the slab failures on the tempo of landscape evolution and resulting landscape morphology. In CHILD, terrain is represented by a triangulated irregular finite volume mesh. Water discharge, sediment transport, and erosion are calculated using Voronoi (Thiessen) polygons that are constructed by intersecting the perpendicular bisectors of each triangle edge. Climate forcing can be simulated stochastically using the Poisson pulse rainfall model of *Eagleson* [1978], where each storm is a discrete random event characterized by a rainfall intensity, duration, and an interstorm period that separates two subsequent storms [*Tucker and Bras*, 2000; *Tucker*, 2004]. The Poisson pulse model uses an exponential probability density function to describe the variability in the climate:

$$f(\eta) = \frac{1}{\eta} e^{(-\eta/\bar{\eta})}. \tag{21}$$

In the model, η takes the respective parameters P, for rainfall intensity, T_r, for duration of rainfall, and T_b, for interstorm duration. The reader is directed to *Tucker et al.* [2001a, 2001b] for detailed information on the CHILD model.

4.2.1. Implementation of the Slab Failure Model in CHILD

[34] In landscape evolution models (see review by *Coulthard* [2001]), calculation of topographic attributes and modeling of sediment and water exchange between model elements (i.e., grid cells, Voronoi cells) are traditionally based on the assumption that the topographic surface, $z(x, y, t)$, represented by a lattice of discrete model elements, is continuous everywhere in the modeled domain at least to the first derivative. There is often no distinction between channels and hillslopes, and geomorphic process laws that predict vertical erosion and deposition [i.e., *Dietrich et al.*, 2003] are applied everywhere in the modeled domain. Most models make no allowance for vertical steps and purely horizontal motion of the modeled surface.

[35] In contrast, a U-shaped gully represents a discontinuity on the topographic surface with distinct vertical walls, termed "scarp face" in the remainder of the paper, that mark a sudden elevation drop of up to tens of meters. In modeling gully erosion numerically, identifying the model cells that host a scarp face is important for at least two reasons. First, in a U-shaped gully the scarp face is subject to lateral retreat in the direction normal to the scarp face in the horizontal plane [*Howard*, 1995]. Second, conventional methods for local slope calculation based on finite differences of elevation rely on the assumption that the surface $z(x, y, t)$ is continuous. This would overestimate the slope for the surface behind the scarp face that is represented by a finite cell size in the model. In real topography, these cells correspond to the top of the gully banks, and in most gullies they form the boundary between the vertical scarp face drop of a gully and a flat valley fill or plateau (Figures 2 and 10).

[36] In the application of the slab failure model in CHILD, the Voronoi polygon edge that lies perpendicular to the triangle edge pointing in the steepest descent direction between a node and its six neighbors is assumed to host the scarp face (Figure 10). A voronoi cell that hosts a scarp face, termed "scarp cell," is identified when the following two criteria are satisfied: (1) local slope is greater than the slope of its downstream cell, assuring slope steepening in the upstream direction, and (2) cell height, estimated as the elevation difference between the cell and its downstream neighbor, is greater than a maximum critical height for slabs with saturated cracks (equation (8)). This is the critical height below which no slab failure occurs. When the scarp face has a greater height, a failure may occur depending on the water level in the tension cracks. Both surface slope and cell height are calculated using elevation at the center of the voronoi cell. Once a scarp cell is identified, stability

Table 1. Parameter Values Used in Model Simulations

Parameter	Value
Mean rainfall rate, $\overline{P}$, mm h^{-1}	15
Mean rainfall duration, $\overline{T}_r$, hours	1.75
Mean interainfall interval, $\overline{T}_b$, days	18.25
Soil cohesion, C, kPa	5, 10, 20
Soil density, ρ_s, kg m^{-3}	1850
Soil friction angle, ϕ, deg	40
Soil infiltration capacity, I_s, mm h^{-1}	10
Angle of the potential failure plane, α, deg	70
Crack infiltration capacity, I_c, m h^{-1}	11
Threshold slope for rapid failures, S_t, %	85
Diffusion constant, K_d, m^2 yr^{-1}	0.001
Soil erodibility, k_e, m yr^{-1}(kg $m^{-1}s^{-2})^{-p}$	1
Critical shear stress, τ_c, Pa	5
Manning's roughness, n	0.03
Erosion exponent, p	2

analysis is conducted only in the scarp cells. If a scarp cell has two or more scarp faces, only the highest one is considered in the slab failure calculations. Local slope of the surface of a scarp cell, S_j is approximated as the average of the gradients between the cell center and its upstream neighbors:

$$S_j = \frac{dz_j}{dx_{i,j}} = -\frac{1}{N_{i,j}} \sum_{i=1}^{N_{i,j}} \frac{(z_j - z_i)}{L_{i,j}}, \qquad (22)$$

where $N_{i,j}$ is the number of upstream nodes draining to node j located at the center of a scarp cell, and $L_{i,j}$ is the length of the triangle edge connecting nodes i and j. This slope is used for vertical runoff erosion calculations at the center of the scarp cell. Experimenting with CHILD using different slope calculation alternatives, we find that starting from an elevated mesa-like surface, scarp faces are maintained when equation (22) is used for slope calculation. Alternative slope calculation algorithms that use forward differences of elevation predict unreasonably high local surface slopes for the scarp cells. This causes the rapid lowering of the scarp cell due to high rates of water erosion and therefore a gully with vertical sidewalls does not form.

[37] During the model operation the factor of safety, FS, is calculated using equation (2), only in the scarp cells. Slab failure occurs when FS is less than 1. The retreat length of the scarp face resulting from each failure is assumed to be the horizontal distance between the scarp face and the tension crack, L_c (Figure 2; equation (4a)). Failed material is deposited in the downstream cell or moves downslope until a stable slope angle, defined by S_t is reached. Once deposited, failed material is subject to surface wash and soil creep. In the scarp cell, retreat length of each failure is incremented. When the accumulated retreat length exceeds the voronoi cell length (Figure 10), the cell is lowered to the elevation of the downstream cell.

4.2.2. Numerical Experiments

[38] In order to understand the geomorphic implications of the interactions between slab failures and fluvial erosion, we present a series of numerical experiments using the CHILD model. As an initial condition we use a rectangular block, 300 m in width and 400 m in length, represented by a Triangulated Irregular Network (TIN) mesh of 5 m node spacing. One side of the block is set as an open boundary, and any sediment reaching this side is assumed to be transported away. The initial surface dips toward the open boundary with an initial gradient of 1%, and is seeded with small random perturbations in the elevation of each node. A 10-m-high scarp face runs along the open boundary. A natural analog to this initial condition would be a rapid incision of a gently sloped valley floor due to knickpoint migration that creates potential scarp faces along the arroyo track [*Bull*, 1997], or it can be considered as a road cut, fault scarp, or a similar feature.

[39] We have considered three different sets of simulations in our analyses. Parameter values used in the simulations are presented in Table 1. All rainfall data are generated using the same random seed to ensure the generation the same rainfall fluctuations in different simulation runs. We use a soil erodibility of 1 m yr^{-1} (kg m^{-1} $s^{-2})^{-p}$, a value close to the reported soil erodibility by *Nearing et al.* [1999] for their field area at the Lucky Hills site of the Walnut Gulch watershed in Tombstone, Arizona. In the numerical experiments, we first vary soil cohesion while holding all other model parameters constant. Climate parameters of the Poisson-pulse model are selected to represent a rainfall regime with short-duration, high-intensity rainfall events, typical of the southwest United States (Table 1). In a second set of runs, we explore the implications of rainfall variability for gully formation by adjusting storm intensity and duration while keeping the time between storms and the total amount of precipitation delivered by each storm constant, so as to create different storm magnitude–frequency characteristics. In the third set of runs, we vary the erosion threshold term, often correlated with vegetation cover, to simulate the effects of the variations in the surface cover on gully erosion.

4.2.2.1. Effects of Soil Cohesion

[40] As field observations demonstrate, development of vertical gully scarps is highly correlated with soil cohesion, either provided by the soil itself as a material property or generated due to an increase in soil suction under unsaturated conditions [e.g., *Collison*, 1996, 2001]. Yet there is very limited knowledge, mostly based on laboratory experiments, of the effects of soil cohesion on the form and tempo of landscape development [*Howard*, 1988; *Howard and McLane*, 1988]. Here we report simulation runs using soil cohesion values of C = 5 kPa, 10 kPa and 20 kPa. For comparison, cohesion of organic clay varies between 10 and 30 kPa [*Selby*, 1993]. Critical scarp height varies as a function of soil cohesion. Under dry conditions, the maximum height before slab failures is 1.6 m, 3.2 m and 6.4 m for the respective soil cohesion values of 5 kPa, 10 kPa and 20 kPa (equation (7)). In the worst case scenario, when cracks are filled with runoff water, the threshold height is one fourth of the maximum height (equation (8)).

[41] Figure 11 shows the modeled landscape mass after each storm event, normalized to the initial mass. In the first time step, mass loss occurs instantaneously due to gravitational failures controlled by soil cohesion in absence of any climate forcing. This rapid initial backwasting of scarp face forms a talus slope and terminates when no unstable scarp face is left. After this initial slope adjustment, the land would remain stable to failures if no water erosion occurred.

[42] All three of the simulations exhibit high rates of soil loss in the first few hundred years (Figure 11). The average mass loss rate in the low-cohesion experiment is

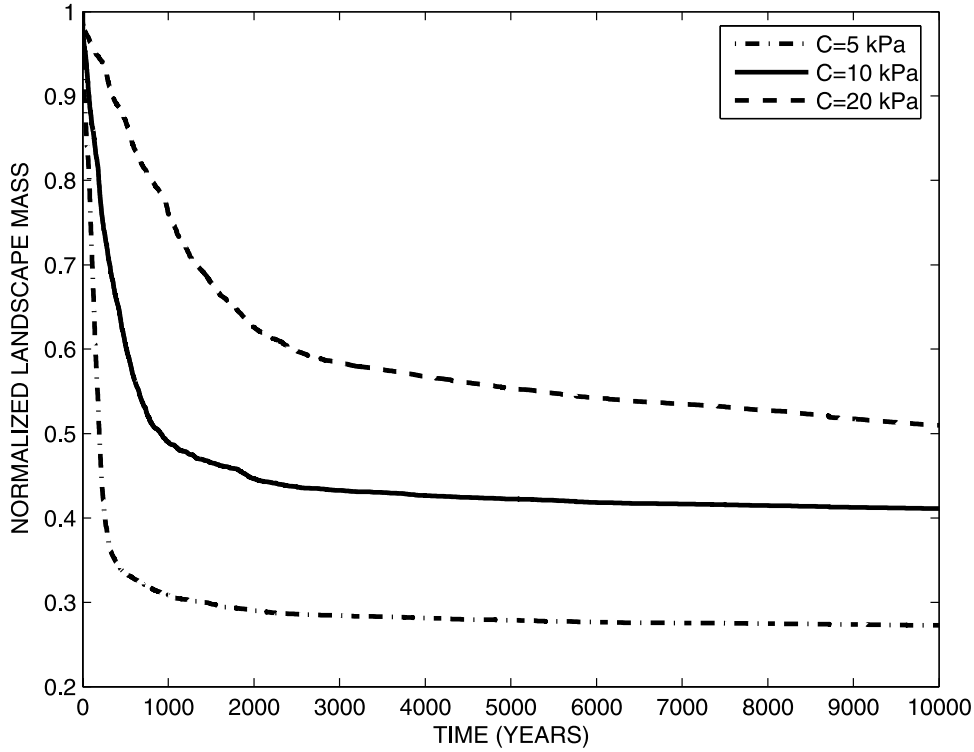

Figure 11. Landscape mass normalized to the initial landscape mass as a function of time for different values of soil cohesion, *C*.

respectively four and thirteen times higher than in the runs with $C = 10$ kPa and 20 kPa. After this rapid soil evacuation, the spatially averaged erosion rate, defined as the rate of mass loss from the entire landscape (i.e., slope of the relationship between the normalized landscape mass as a function of time), settles to an approximately constant rate. In the simulations, the lower the soil cohesion, the higher the erosion rate. Because we use a fixed value for soil erodibility and climate forcing in all cases, differences in the erosion rates suggest organizational differences in the eroded topography. To illustrate this we plot landscape topography after 20% of the initial mass has been eroded in each of the simulations (Figures 12a, 12b, and 12c). These landscapes correspond to model times of approximately 100 years, 200 years and 1100 years for the low-, medium-, and high-cohesion simulations, respectively. If soil cohesion had no effect on the landscape morphology and organization beyond speeding up soil loss, then all three plotted topographies would look alike.

[43] The low-cohesion simulation pictured in Figure 12a shows the case in which sediment released by gravitational failures eliminates the scarp face. In this simulation, flow convergence has a limited effect in scarp retreat as the critical scarp height for failures is low even in dry conditions. This creates a line of continuous scarp faces across the width of the simulation domain that travels at an approximately constant backwasting rate. This is similar to the one-dimensional model simulation in Figure 9b, with one difference being that topography is not completely erased in the lower regions in the CHILD runs because of an erosion threshold. Valleys are formed in the talus deposits by the action of slope wash and soil creep and no unstable scarp faces are left behind. The model produces broad valleys typical of wash dominated landscapes on loose soils, instead of developing gullies with steep sidewalls.

[44] The other end-member simulation is the case with $C = 20$ kPa (Figure 12c). In this simulation, the critical scarp height for failures is approximately 4 times higher than that of the low soil cohesion simulation in Figure 12a. Within the first time step of this simulation, toe deposits accumulate enough sediment that would put scarps into a "conditionally stable" state, in which failures only occur during large storm events. In some cases the scarp heights fall below the minimum critical height, when cracks are entirely filled with water at which point, they remain stable unless the toe deposit is eroded. Therefore gully erosion can propagate headward only at the tips of the gullies where flow convergence is high and fluvial erosion is more active in eroding the toe deposits. This results in a highly dissected topography compared to the low soil cohesion case in Figure 12a. The intermediate case represents soil cohesion at $C = 10$ kPa. This simulation shows significant channel widening that erases the overheightened sidewalls along major valleys as valleys preferentially grow toward regions with high flow convergence (Figure 12b).

[45] *Howard* [1988] studied landform development driven by groundwater sapping using a 5 feet square and 2 feet deep aluminum tank with a head-controlled upstream reservoir. Using cohesionless and slightly cohesive sand material, *Howard* [1988] observed the growth of small-scale gullies due to backwasting of gully walls primarily driven by undermining by seepage erosion and episodic mass-

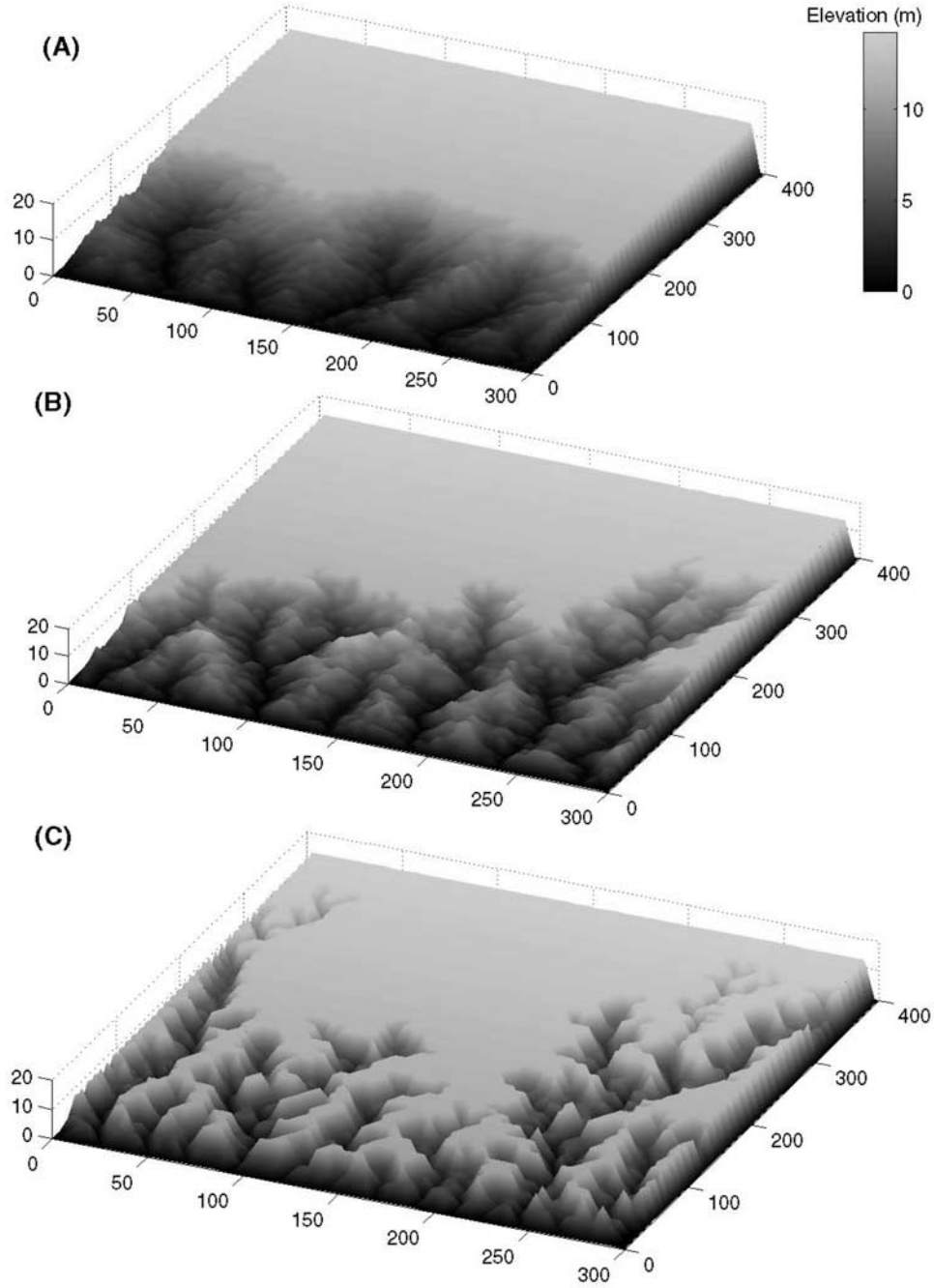

Figure 12. Topography after 20% of the initial mass is eroded. Values of soil cohesion area are (a) C = 5kPa, (b) C = 10 kPa, and (c) C = 20 kPa. Lengths are in meters. The color scale represents elevations and is the same for all three figures.

wasting processes. Wide gullies developed in cohesionless soils. Introducing cohesion in the experiments resulted with the development of narrower, but deeper valleys and more dendritic gully networks. Erosion rates were observed to be significantly lower in the case of cohesive material than with cohesionless sand. Our modeling results are in agreement with the experimental results of *Howard* [1988].

4.2.2.2. Changes in Storm Characteristics

[46] It has been suggested that differences in storm characteristics, such as storm intensity, frequency and seasonality, rather than the mean annual precipitation, are the primary factors in arroyo development in the southwestern United States [*Leopold*, 1951; *Balling and Wells*, 1990] and may in fact be the key drivers in many fluvial systems [e.g., *Tucker and Bras*, 2000; *Molnar*, 2001; *Tucker*, 2004]. Here we illustrate the potential consequences of rainfall variability for gully development by altering the mean rainfall intensity and duration reported in Table 1, while keeping the mean annual precipitation approximately constant. This allows us to explore the sensitivity of gully development to storm

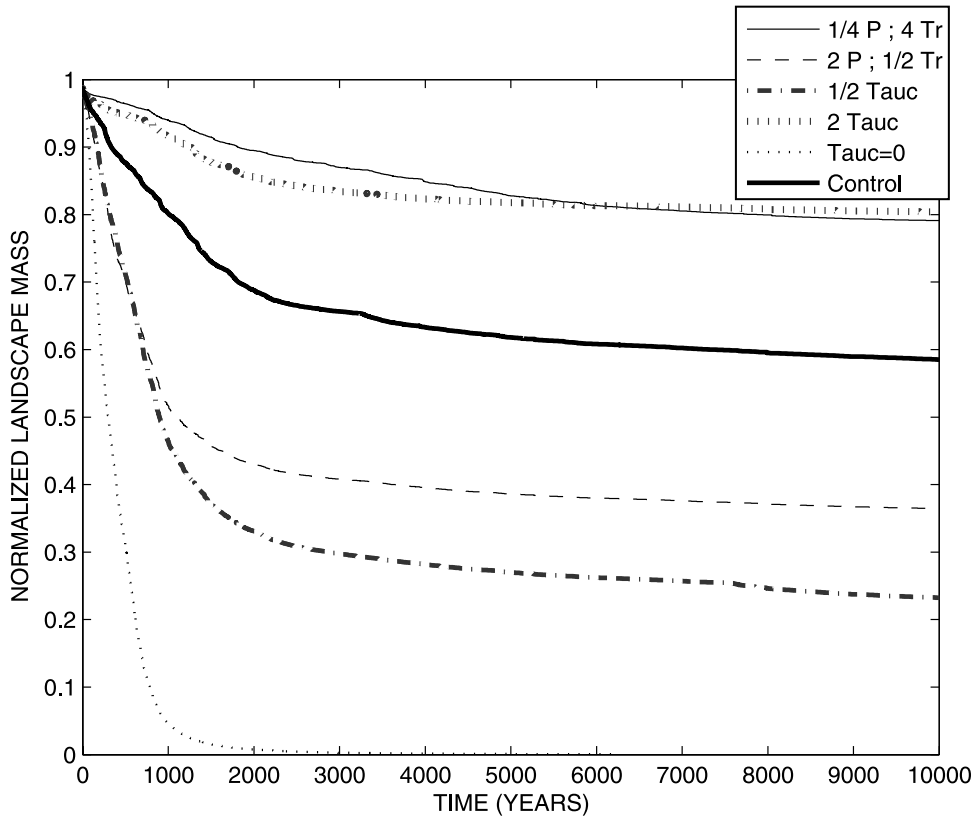

Figure 13. Landscape mass normalized to the initial landscape mass as a function of time for the simulations with changes in climate forcing, where P is rainfall rate and T_r is storm duration, and critical shear stress, τ_c, compared to the control simulation.

intensity-duration characteristics. In the first simulation, we reduce the mean rainfall rate, $\overline{P}$, fourfold with an accompanying fourfold increase in rainfall duration, $\overline{T}_r$, so that $\overline{P}$ = 3.8 mm/hr and $\overline{T}_r$ = 7 hours. The low-intensity, long-duration storms generated in this simulation are typical of cyclonic weather conditions. In the second simulation, we doubled the mean rainfall rate and halved the mean storm duration so that $\overline{P}$ = 30 mm/hr and $\overline{T}_r$ = 0.88 hours, in order to produce high-intensity, short-duration storms similar to convective thunderstorms associated with monsoon climate typically observed in the southwestern United States.

[47] Soil cohesion is set to 20 kPa in all simulations, and the model run with C = 20 kPa reported in Figures 11 and 12c is used as the control run. Figure 13 plots the normalized landscape volume as a function of time for all the runs. Figures 14a and 14b show the topographic effects of rainfall variability after 20% of mass loss in the low-intensity, long-duration and high-intensity, short-duration simulations, respectively (these correspond to model times of 7980y and 307y).

[48] Despite no change in the total rainfall depth delivered by each storm, an increase in mean rainfall rate speeds up erosion. The high-intensity, short-duration simulation exhibits high rates of mass loss in the first 1000 years, with an average loss rate approximately 2.5 times higher than the control case. In the case of low-intensity, long-duration simulation, landscape mass decays monotonically without any sharp transition from high rates to low ones. In this experiment, a fourfold reduction in rainfall rate leads to a sevenfold decrease in the erosion rate during the removal of the first 20% of the initial mass.

4.2.2.3. Changes in Erosion Threshold

[49] In order to simulate the effects of erosion threshold, τ_c, on gully development, three simulations with a twofold increase, a twofold decrease, and no threshold are carried out. Here an increase in the erosion threshold corresponds to denser surface vegetation [i.e., *Prosser et al.*, 1995]. No erosion threshold implies a bare soil surface of very fine, easily detachable material.

[50] Landscape response to changes in erosion threshold is very similar in style, but in the opposite direction, to modeled changes in rainfall rate. Lowering the erosion threshold enhances widespread gullying due to increased fluvial activity. High rates of runoff erosion both reduces the spacing between gullies, and increases the rate of gully widening by rapidly removing the failed scarp deposits. Absence of any threshold completely removes the initial topography in 3000 years (Figure 13). Figures 15a and 15b show the impact of a twofold increase in the erosion threshold in different times. Doubling the erosion threshold reduces the initial high erosion rates in the first 2000 years (Figure 13) by more than threefolds relative to the control case, at which time, 12% of the initial mass has been consumed by gully erosion (Figure 15a). After this time, gullying essentially stops in this simulation, and diffusive processes and infrequent wash erosion shape the landscape. Figure 15b shows the landscape after 20% of

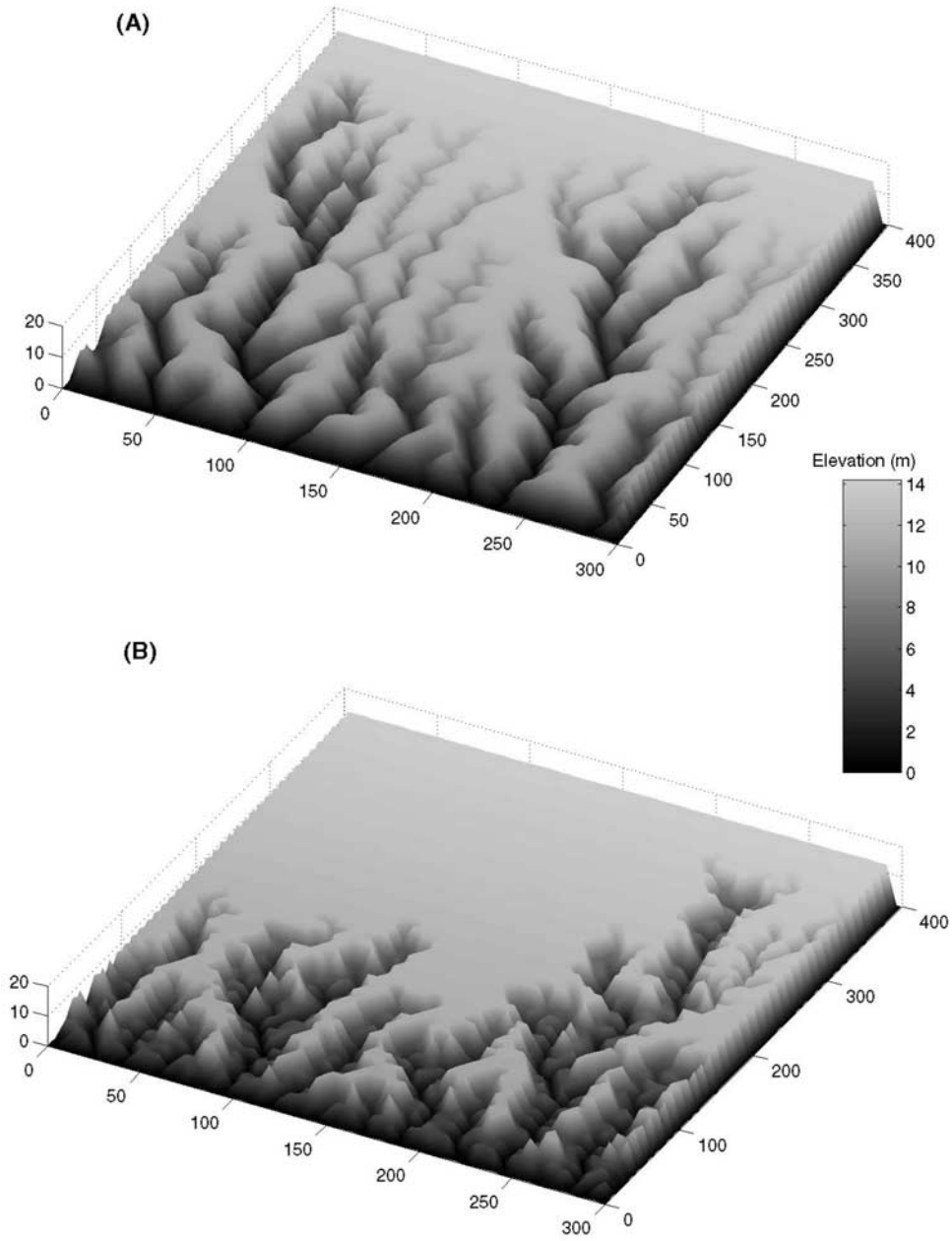

Figure 14. Topography after 20% of the initial mass is eroded. (a) Climate driven by low-intensity, long-duration storms. (b) Climate driven by high-intensity, short-duration storms. In both simulations, soil cohesion is 20 kPa, and mean annual precipitation is constant.

the initial mass has been eroded. The rounded hilltops are typical of diffusion dominated landscapes.

[51] In the model, both runoff and erosion calculations are based on the exceedence of a threshold term. When this threshold-dependent erosion model is solved with storms of randomly varying magnitudes, a decrease in the mean rainfall rate leads to less frequent runoff generation with lower runoff rates, reducing both the number of erosive floods and their erosivity everywhere in the basin compared to the control run. This is also the case when the erosion threshold is increased. These findings can also be discussed on the basis of the derived theory. The critical threshold area for erosion initiation, A_c that is the upslope area of a point where $\tau = \tau_c$ for a given slope, and the erosion rate scale with runoff rate and critical shear stress as

$$A_c \propto \tau_c^{1/m} R^{-1} \tag{23}$$

$$E \propto \left(\gamma R^{mp} - \tau_c^p\right) T_r \qquad \forall m < 1, \qquad p > 1. \tag{24}$$

[52] Both in the case of an increase in the critical shear stress or reduction in the runoff rate a greater drainage area is required for erosion initiation. Thus, although slab failures occur, especially in the beginning of the simulations as in Figure 15a, side scarps in gullies stabilize quite

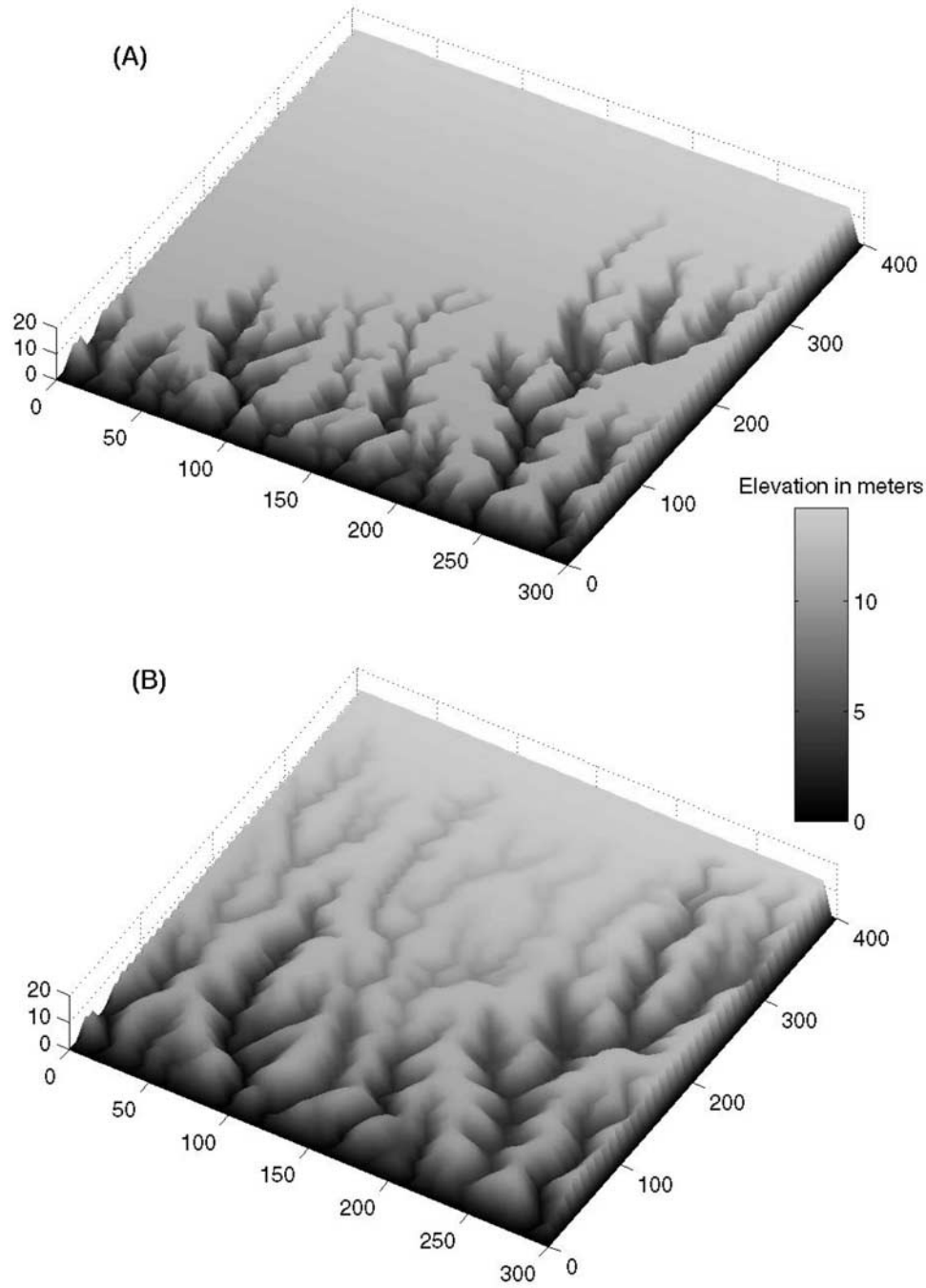

Figure 15. Topography at two different times during the simulation with twofold increase in the erosion threshold. (a) After 12% of the initial mass is eroded. (b) After 20% of the initial mass is eroded. Soil cohesion is 20 kPa in both cases.

rapidly due to lack of soil removal from the toe deposits. Reduced fluvial erosion in time and space leads to the elimination of scarp faces, and the development of smooth, rounded hilltops due to continuous diffusive processes (Figures 14a and 15b). Sensitivity of sediment transport and erosion formulations to variability in rainfall rate and mean annual precipitation has been demonstrated by *Tucker and Bras* [2000], who found a greater sensitivity between erosion and rainfall characteristics when thresholds for runoff generation and particle detachment are significant and erosion is highly nonlinear with shear stress.

[53] Erosion is nonlinearly related to runoff rate and its sensitivity to storm rate and duration depends on model exponents. For example, for all $p > 1/m$, a change in rainfall rate may require a greater change in storm duration in the opposite direction to maintain a constant erosion rate. Because $mp > 1$ in the simulations, erosion would occur less frequently but also with lower magnitudes in the low-intensity, long-duration simulation and more frequently with higher magnitudes in the high-intensity, short-duration experiment compared to the control case. This is among the reasons why large gullies in Figure 14b (time: 307 years)

Table 2. Summary of the Model Results

Model Parameter	Low	High
Soil cohesion[a]	1. low-threshold scarp height for failures 2. rapid valley widening by small failures 3. high rates of soil loss 4. shaping of the topography by soil wash 5. low landscape dissection	1. high threshold scarp height 2. development of U-shaped gullies with steep sidewalls 3. slow rates of soil loss 4. high landscape dissection
Rainfall intensity[b]	1. reduced runoff erosion 2. larger distance between gullies 3. reduced rate of slab failures 4. termination of slab failures due to lack of failure deposit removal 5. shaping of the topography by hillslope diffusion and reduced runoff erosion	1. increased runoff erosion 2. smaller distance between gullies 3. slab failures enhanced by erosion of failure deposits 4. erosion of the bank tops 5. termination of slab failures when vertical bank height is below threshold 6. shaping of the topography by soil wash
Erosion threshold[c]	same as high rainfall intensity	same as low rainfall intensity.

[a]For climate driven by short-duration, high-intensity storms.
[b]For high soil cohesion and a moderate erosion threshold.
[c]For climate driven by short-duration, high-intensity storms and high soil cohesion.

develop approximately four times more rapidly than those in Figure 12c (time: 1100 years). Note that in both figures the topography contains equal amount of mass. It is important to note also that CHILD solves elevation change during a storm using an adaptive time-stepping scheme [*Tucker et al.*, 2001a, 2001b], hence erosion duration can be smaller than storm duration in the case when a slope flattens quite rapidly.

[54] The model is more sensitive to changes in erosion threshold than in the rainfall characteristics. A twofold increase in the erosion threshold ($2\tau_c$) has a greater control on gully erosion than a fourfold decrease in the mean storm rate ($1/4\ \overline{P}$ and $4\ \overline{T}_r$) due to the nonlinearity of the process as outlined in equations (23) and (24). In the high-intensity, short-duration ($2\ \overline{P}$ and $1/2\ \overline{T}_r$), and low-threshold ($1/2\tau_c$) simulations, although the rate of soil loss is approximately equal in the first 1000 years in both experiments, reduction in erosion rates takes place more slowly in the low-threshold simulation leading to higher erosion totals at the end of the model run. Comparison of Figures 14a (low-intensity, long-duration simulation) and 15b (high erosion threshold simulation) also show differences in the topography. Landscape is less dissected, with shallow channels and rounded hillslopes by slope-dependent soil creep when the erosion threshold is high compared to lower rainfall rate. Note that in both figures gully erosion is no longer an active process in shaping the landscape.

[55] In the previous section, our model results related gully cross-sectional shape to soil cohesion. Although in agreement with field observations, this conclusion may only be valid for actively eroding gullies. Gullies pictured in both Figures 14a and 15b are no longer subject to mass failures. However, in both cases gully erosion began at the open model boundary, and incision of U-shaped gullies (i.e., Figure 15a) continued until flow shear stress fell below the threshold value near the banks.

5. Summary and Conclusions

[56] In this paper we have explicitly formulated and addressed the topographic implications of gravitational slab failures along channel banks in landscape evolution modeling. Characterizing in-channel processes in landscape evolution models is an important step in understanding the factors that control gully erosion and river channel instability, as well as predicting the type of channel response and its timescales to changes in external factors such as climate and land use. The slab failure theory presented in this paper predicts the limiting scarp height as a function of soil cohesion and soil water depth in the tension cracks that develop at the back of the scarp face. Relating water in the tension crack to surface runoff discharge gives the limiting scarp height as a function of unit contributing area. We have tested the essence of the theory using field measurements of scarp heights and soil cohesions in a gully system in Fort Carson, Colorado. Using adjusted soil cohesion information obtained in the field, the model explains 60% of the observed variability in scarp heights in the field, pointing out the importance of soil cohesion and its variability in time and space in maintaining vertical gully banks. Gully headcut depth, width and upslope contributing area data reported by *Nyssen et al.* [2002] provide an additional test to the model. Calibration of the theory in the upslope area-scarp height space using different soil cohesion values with a fixed hydrology parameter, Ω, explains the trend between headcut height and upslope drainage area observed by *Nyssen et al.* [2002].

[57] Simulation experiments using a one-dimensional profile evolution model show the implications of coupling fluvial erosion and gravitational processes on the type of retreat (i.e., parallel backwasting, slope replacement) and morphology of the retreating profile. Compared to a strictly fluvial case, including gravitational processes in the 1-D model produced a distinct morphology characterized by a vertical scarp face and a talus slope as extensively documented in the field where gravitational failure processes operate [*Selby*, 1993]. Increased nonlinearity in the runoff erosion (i.e., a higher shear stress exponent) leads to the dominance of slope replacement in talus evolution over parallel retreat (e.g., Figure 8c) and more rapid removal of the scarp face. Observed gully bank profiles compare well with the one-dimensional retreat model simulations, suggesting that gully morphology can be potentially used

to decipher the nonlinearity of wash erosion in the field (Figure 9).

[58] Slab failures have profound effects on the tempo of topographic evolution. Numerical simulations conducted using the CHILD model underscore the importance of three key environmental factors in gully erosion; soil cohesion, climate forcing and erosion threshold. Results from the sensitivity analysis of the CHILD model to variations in these parameters are summarized in Table 2. In the simulations, initial high rates of erosion, as a response to sudden base-level drop, continue until either the upward expansion of the talus slope covers the scarp, or the scarp face retreats to a point where the scarp height is significantly lower than the minimum failure threshold. The former occurs in the case of less cohesive soils, when the rate of soil release from the scarp face by slab failures is significantly higher than the rate of soil removal from the talus. Thus the talus slope expands rapidly and stabilizes the scarp face, whereupon wash erosion and hillslope diffusion shapes the landscape. When the soil cohesion is high, soil release from the scarp face is slower than soil loss from the toe of the gully bank due to higher height thresholds, causing deeper and narrower U-shaped gullies with toe deposits. In addition, channels tend to grow headward, developing a more dissected topography when the soil cohesion is high.

[59] Numerical experiments reported in this paper stress the importance of high-intensity thunderstorms in the tempo of gully development. In the model, flow shear stress is directly related to excess rainfall intensity, thus the erosion threshold in gullies is exceeded more frequently in a climate regime characterized by high-intensity thunderstorms. Rapid flash floods generated during these thunderstorms clean out the debris that had slumped into the channel from the headcut and sidewalls.

[60] The erosion threshold is found to have a similar effect on gully development, but in the opposite direction, with rainfall rate. The model suggests a greater sensitivity in landscape response to erosion thresholds than to storm rate. This conclusion is also consistent with the theoretical arguments by *Tucker and Slingerland* [1997].

[61] As a first attempt in explicitly modeling gully erosion we have focused on describing the physical basis for gully development by sidewall failures and water erosion. Other landscape processes that play a role in gully erosion, including piping and plunge pool erosion that directly undercuts gully walls and headcuts remain to be incorporated in the model.

[62] In the simulation experiments reported, we assumed no spatial and temporal variability in the model parameters. As our field observations also suggest, both soil cohesion and potentially the erosion threshold would show a significant variation on the landscape. Soils are heterolithic and texturally diverse substrate of loess, alluvium and paleosols. Such heterogeneities on the landscape properties may have important implications on gully development. It is conceivable that with variability in soil cohesion, headward growth of gullies would perhaps follow the paths of less cohesive materials on the landscape, and form channels with variable sidewall heights. Issues related to heterogeneities on the landscape properties, including soils and vegetation, and in climate and tectonic forcing of the system in space and time still remain to be resolved in the future. Such issues can be address through a balanced combination of field studies and modeling process interactions.

[63] **Acknowledgments.** This work is funded by the U.S. Army Research Office contract DAAD19-01-1-0513 and by the Italian National Research Council. We thank John F. Pazzaglia and Alex Densmore for their invaluable comments that improved this manuscript and Nicole Gasparini for her help in code design.

References

Balling, R. C., and S. G. Wells (1990), Historical rainfall patterns and arroyo activity within the Zuni River drainage basin, New Mexico, *Ann. Assoc. Am. Geogr.*, *80*, 603–617.

Bennett, S. J., C. V. Alonso, S. N. Prasad, and M. J. M. Römkens (2000), Experiments on headcut growth and migration in concentrated flows typical of upland areas, *Water Resour. Res.*, *36*, 1911–1922.

Bradford, J. M., and R. F. Piest (1980), Erosional development of valley-bottom gullies in the upper midwestern United States, in *Thresholds in Geomorphology*, edited by D. R. Coates and J. D. Vitek, pp. 75–101, Allen and Unwin, St. Leonards, NSW, Australia.

Bull, W. B. (1997), Discontinuous ephemeral streams, *Geomorphology*, *19*, 1109–1124.

Collison, A. (1996), Unsaturated strength and preferential flow as controls on gully head development, in *Advances in Hillslope Processes*, edited by M. G. Andersen and S. M. Brooks, pp. 753–769, John Wiley, Hoboken, N. J.

Collison, A. J. C. (2001), The cycle of instability: Stress release and fissure flow as controls on gully head retreat, *Hydrol. Processes*, *15*, 3–12.

Cooke, R. U., and R. W. Reeves (1976), *Arroyos and Environmental Change in the American Southwest*, 213 pp., Clarendon, Oxford, U. K.

Coulthard, T. J. (2001), Landscape evolution models: A software review, *Hydrol. Processes*, *15*, 165–173.

Croke, J., and S. Mockler (2001), Gully initiation and road-to-stream linkage in a forested catchment, southeastern Australia, *Earth Surf. Processes Landforms*, *26*, 205–217.

Dapporto, S., M. Rinaldi, N. Casagli, and P. Vannocci (2003), Mechanisms of riverbank failure along the arno river, central Italy, *Earth Surf. Processes Landforms*, *28*, 1303–1323.

Darby, S. E., and C. R. Thorne (1996), Development and testing of riverbank-stability analysis, *J. Hydraul. Eng.*, *122*, 443–454.

Darby, S. E., A. M. Alabyan, and M. J. Van de Wiel (2002), Numerical simulation of bank erosion and channel migration in meandering rivers, *Water Resour. Res.*, *38*(9), 1163, doi:10.1029/2001WR000602.

Densmore, A. L., M. A. Ellis, and R. S. Anderson (1998), Landsliding and the evolution of normal-fault-bounded mountains, *J. Geophys. Res.*, *103*, 15,203–15,219.

Dietrich, W. E., and T. Dunne (1993), The channel head, in *Channel Network Hydrology*, edited by K. Beven and M. J. Kirkby, pp. 175–219, John Wiley, Hoboken, N. J.

Dietrich, W. E., D. Bellugi, A. M. Heimsath, J. J. Roering, L. S. Sklar, and J. D. Stock (2003), Geomorphic transport laws for predicting landscape form and dynamics, in *Predictions in Geomorphology*, *Geophys. Monogr. Ser.*, vol. 135, edited by P. R. Wilcock and R. M. Iverson, pp. 1–30, AGU, Washington, D. C.

Dodge, R. E. (1902), Arroyo formation, *Science*, *15*, 746.

Dunne, T. (1980), Formation and control of channel networks, *Prog. Phys. Geogr.*, *4*, 211–239.

Eagleson, P. S. (1978), Climate, soil and vegetation: 2. The distribution of annual precipitation derived from observed storm sequences, *Water Resour. Res.*, *14*, 713–721.

Graf, W. L. (1979), The development of montane arroyos and gullies, *Earth Surf. Processes Landforms*, *4*, 1–14.

Gupta, H. V., S. Sorooshian, and P. O. Yapo (1998), Toward improved calibration of hydrologic models: Multiple and noncommensurable measures of information, *Water Resour. Res.*, *34*, 751–763.

Higgins, C. G. (1990), Gully development, with a case study by Hill, B. R., and Lehre A. K., *Spec. Pap. Geol. Soc. Am.*, *252*, 139–155.

Howard, A. D. (1980), Thresholds in river regimes, in *Thresholds in Geomorphology*, edited by D. R. Coates and J. D. Vitek, pp. 227–258, Allen and Unwin, St. Leonards, NSW, Australia.

Howard, A. D. (1988), Groundwater sapping experiments and modeling, in *Sapping Features of the Colorado Plateau: A Comparative Planetary Geology Field Guide*, edited by A. D. Howard, R. C. Kochel, and H. E. Holt, pp. 71–83, NASA Sci. and Tech. Inf. Div., Washington, D. C.

Howard, A. D. (1994), A detachment-limited model of drainage basin evolution, *Water Resour. Res.*, *30*, 2261–2285.

Howard, A. D. (1995), Simulation modeling and statistical classification of escarpment planforms, *Geomorphology*, *12*, 187–214.

Howard, A. D. (1999), Simulation of gully erosion and bistable landforms, in *Incised River Channels*, edited by S. E. Darby and A. Simon, pp. 277–299, John Wiley, Hoboken, N. J.

Howard, A. D., and C. F. McLane III (1988), Erosion of cohesionless sediment by groundwater seepage, *Water Resour. Res.*, *24*, 1659–1674.

Istanbulluoglu, E., D. G. Tarboton, R. T. Pack, and C. Luce (2002), A probabilistic approach for channel initiation, *Water Resour. Res.*, *38*(12), 1325, doi:10.1029/2001WR000782.

Kirkby, M. J. (1971), Hillslope process-response models based on the continuity equation, *Inst. Br. Geogr. Spec. Publ.*, *3*, 15–30.

Kirkby, M. J., and L. J. Bull (2000), Some factors controlling gully growth in fine-grained sediments: A model applied in southeast Spain, *Catena*, *40*, 127–146.

Kirkby, M. J., L. J. Bull, J. Poesen, J. Nachtergaele, and L. Vanderkerckhove (2003), Observed and modeled distributions of channel and gully heads with examples from SE Spain and Belgium, *Catena*, *50*, 415–434.

Leopold, L. B. (1951), Rainfall frequency: An aspect of climate variation, *Eos Trans. AGU*, *32*, 347–357.

Molnar, P. (2001), Climate change, flooding in arid environments, and erosion rates, *Geology*, *29*, 1071–1074.

Montgomery, D. R. (1999), Erosional processes at an abrupt channel head: Implications for channel entrenchment and discontinuous gully formation, in *Incised River Channels: Processes, Forms, Engineering and Management*, edited by S. E. Darby and A. Simon, pp. 247–276, John Wiley, Hoboken, N. J.

Montgomery, D. R., and W. E. Dietrich (1994), Landscape dissection and drainage area-slope thresholds, in *Process Models and Theoretical Geomorphology*, edited by M. J. Kirkby, pp. 221–246, John Wiley, Hoboken, N. J.

Mosley, M. P. (1972), Evolution of a discontinuous gully system, *Ann. Assoc. Am. Geogr.*, *63*, 655–663.

Nearing, M. A., J. R. Simanton, L. D. Norton, S. J. Bulygin, and J. Stone (1999), Soil erosion by surface water flow on a stony, semiarid hillslope, *Earth Surf. Processes Landforms*, *24*, 677–686.

Nyssen, J., J. Poesen, J. Moeyersons, E. Luyten, M. Veyret-Picot, J. Deckers, M. Haile, and G. Govers (2002), Impact of road building on gully erosion risk: A case study from the northern Ethiopian highlands, *Earth Surf. Processes Landforms*, *27*, 1267–1283.

Osborn, H. B., and J. R. Simanton (1986), Gully migration on a southwest rangeland watershed, *J. Range Manage.*, *39*, 558–561.

Poesen, J., J. Nachtergaele, G. Verstraeten, and C. Valentin (2003), Gully erosion and environmental change: Importance and research needs, *Catena*, *50*, 91–133.

Prosser, I. P., and M. Soufi (1998), Controls on gully formation following forest clearing in a humid temperate environment, *Water Resour. Res.*, *34*, 3661–3671.

Prosser, I. P., W. E. Dietrich, and J. Stevenson (1995), Flow resistance and sediment transport by concentrated overland flow in a grassland valley, *Geomorphology*, *13*, 71–86.

Roering, J. J., J. W. Kirchner, and W. E. Dietrich (1999), Evidence for nonlinear, diffusive sediment transport on hillslopes and implications for landscape morphology, *Water Resour. Res.*, *35*, 853–870.

Rosenbloom, N. A., and R. S. Anderson (1994), Hillslope and channel evolution in a marine terraced landscape, Santa Cruz, California, *J. Geophys. Res.*, *99*, 14,013–14,029.

Schmidt, K. M., and D. R. Montgomery (1995), Limits to relief, *Science*, *270*, 617–620.

Schumm, S. A. (1999), Causes and controls of channel incision, in *Incised River Channels*, edited by S. E. Darby and A. Simon, pp., 19–33, John Wiley, Hoboken, N. J.

Schumm, S. A., and R. S. Parker (1973), Implications of complex response of drainage systems for Quaternary alluvial stratigraphy, *Nature*, *243*, 99–100.

Schumm, S. A., M. D. Harvey, and C. C. Watson (1984), *Incised Channels: Morphology, Dynamics and Control*, 200 pp., Water Resour. Publ., Highlands Ranch, Colo.

Schumm, S. A., M. P. Mosley, and W. E. Weaver (1987), *Experimental Fluvial Geomorphology*, John Wiley, Hoboken, N. J.

Selby, M. J. (1993), *Hillslope Materials and Processes*, 451 pp., Oxford Univ. Press, New York.

Simon, A., and S. E. Darby (1997), Process-form interactions in unstable sand-bed river channels: A numerical modeling approach, *Geomorphology*, *21*, 85–106.

Simon, A., A. Curini, S. E. Darby, and E. J. Langendoen (2000), Bank and near-bank processes in an incised channel, *Geomorphology*, *35*, 193–217.

Thorne, C. R. (1999), Bank processes and channel evolution in the incised rivers of north-central Mississippi, in *Incised River Channels*, edited by S. E. Darby and A. Simon, pp. 97–121, John Wiley, Hoboken, N. J.

Tucker, G. E. (2004), Drainage basin sensitivity to tectonic and climatic forcing: Implications of a stochastic model for the role of entrainment and erosion thresholds, *Earth Surf. Processes Landforms*, *29*, 185–205.

Tucker, G. E., and R. L. Bras (1998), Hillslope processes, drainage density, and landscape morphology, *Water Resour. Res.*, *34*, 2751–2764.

Tucker, G. E., and R. L. Bras (2000), A stochastic approach to modeling the role of rainfall variability in drainage basin evolution, *Water Resour. Res.*, *36*, 1953–1964.

Tucker, G. E., and R. Slingerland (1997), Drainage basin responses to climate change, *Water Resour. Res.*, *33*, 2031–2047.

Tucker, G. E., and K. X. Whipple (2002), Topographic outcomes predicted by stream erosion models: Sensitivity analysis and intermodel comparison, *J. Geophys. Res.*, *107*(B9), 2179, doi:10.1029/2001JB000162.

Tucker, G. E., S. T. Lancaster, N. M. Gasparini, and R. L. Bras (2001a), The channel-hillslope integrated landscape development model, in *Landscape Erosion and Evolution Modeling*, edited by R. S. Harmon and W. W. Doe, pp. 349–388, Springer, New York.

Tucker, G. E., S. T. Lancaster, N. M. Gasparini, and R. L. Bras (2001b), An object-oriented framework for hydrologic and geomorphic modeling, *Comput. Geosci.*, *27*, 959–973.

Weissel, J. K., and M. A. Seidl (1998), Inland propagation of erosional escarpments and river profile evolution across the southeast Australia passive continental margin, in *Rivers Over Rock: Fluvial Processes in Bedrock Channels*, *Geophys. Monogr. Ser.*, vol. 107, edited by E. Wohl and K. Tinkler, pp. 189–206, AGU, Washington, D. C.

Wemple, B. C., J. A. Jones, and G. E. Grant (1996), Channel network extension by logging roads in two basins, western cascades, Oregon, *Water Resour. Bull.*, *32*, 1195–1207.

Whipple, K. X., and G. E. Tucker (1999), Dynamics of the stream-power river incision model: Implications for height limits of mountain ranges, landscape response timescales, and research needs, *J. Geophys. Res.*, *104*, 17,661–17,674.

Willgoose, G., R. L. Bras, and I. Rodriguez-Iturbe (1991), A coupled channel network growth and hillslope evolution model: 1. Theory, *Water Resour. Res.*, *27*, 1671–1684.

R. L. Bras, H. Flores-Cervantes, and E. Istanbulluoglu, Department of Civil and Environmental Engineering, Massachusetts Institute of Technology, Cambridge, MA 02139, USA. (rlbras@mit.edu; homefc@mit.edu; erkan@mit.edu)

G. E. Tucker, Cooperative Institute for Research in Environmental Sciences, 216 UCB, University of Colorado, Boulder, CO 80309-0216, USA. (gregory.tucker@colorado.edu)